

UNIVERSITY OF BRISTOL

ALEXANDER CROOT

---

# Negative Electron Affinity Diamond for Electrochemical Water Splitting

---

*Supervisor:*

Dr. Neil Fox

*Section:*

*Second assessor:*

Physical & Theoretical Chemistry

Prof. David Fermin

*A thesis submitted in partial fulfilment of the requirements  
for the Honours degree of MSci in Chemical Physics*

*in the*

School of Chemistry

University of Bristol

April 2014

## Abstract

Renewable hydrogen production could form part of a solution to the ever-worsening world energy crisis. Many areas of current research focus on the splitting of water by introduction of energy from green sources such as solar radiation. Diamond is an unconventional material for photoelectrochemistry, but can be excited by UV light and also by beta radiation. If the conduction band energy of a material is higher than that of the vacuum, then it is said to have a negative electron affinity (NEA) and can readily eject electrons with high energy into the surroundings. It is hypothesised that this effect could provide a powerful beta-/photo-cathode. The current project examines the use of NEA diamond as an electrode for water splitting by high energy radiation.

Fabrication of thin layers of highly boron-doped conducting diamond (BDD) on titanium substrates by a polymer self-assembly method yielded robust photoelectrodes. Fine-tuning of seven parameters in the self-assembly process provided optimised diamond layers for use in photoelectrochemistry. These Ti/TiC/BDD structured samples were treated to produce oxygen and oxygen-lithium terminated surfaces, which have positive and negative electron affinities, respectively. These, along with highly porous hydrogen terminated Ti/carbon nanotube (CNT)/BDD structured samples of varied boron doping concentration, formed a set of four test samples, 0.1H, 0.2H, O and OLi.

Cyclic voltammetric measurements revealed bias potential ( $E$ ) windows, over which electrochemical processes were absent, for each sample in three electrolytes: KCl, Na<sub>2</sub>SO<sub>3</sub> and EuCl<sub>3</sub>. Photoelectrochemical measurements were possible within these windows, utilising various techniques. Chronoamperometry provided a measure of photocurrent time evolution when illuminated by a Xe arc lamp. These results showed that two distinct processes were occurring, and that in general they were independent in both sign and timescale. The 'spike' and 'decay' properties of each sample differed greatly, especially when measured in multiple electrolytes. Similar measurements with Ar-Hg discharge illumination rendered photocurrent spikes more prominent than the subsequent decay, allowing lock-in amplified photocurrent detection. Photocurrent-voltage spectra showed linear plots consistent with the metallic conductivity (degeneracy) of the diamond electrodes, and their ability to both oxidise and reduce solution species at different potentials. Efficiency-wavelength spectra showed that photocurrent was stimulated by photons of energy  $> 2.7$  eV, indicating that mid-band-gap surface states are highly active under illumination.

Due to the dual process photocurrent it has been challenging to ascertain the exact photoelectrochemical properties of the three surface terminations. Further work is required to gauge the qualitative differences between the O and OLi terminated samples as results showed few differences, suggesting that the lithiation had limited success. However, the illumination was unlikely to cause inter-band excitation, and was therefore not able to access the unique advantages of the NEA surfaces.

## *Acknowledgements*

Firstly, I would like to thank my supervisor, Dr. Neil Fox for his invaluable support, patience and insight during my project, and for allowing me to undertake it with him. My thanks also go to Prof. David Fermin for his support, many valuable conversations regarding my work, and allowing me to use his lab. In addition, to Prof. Paul May for allowing me use of his lab.

Thank you to Dave, Sarah, Daniela, Kieren and the whole electrochemistry and diamond groups, who took me in and offered their assistance and support wherever possible. Special thanks go to Daniela for her help with my report and to Kieren for giving up so much of his time and always being willing to help.

My thanks go to Dr. Hudson Zanin for donation of his samples, and for his valuable discussions. Thanks to John Rowden, for his skills in the glass workshop.

Many thanks to Dev Panchal for sharing diamond samples and DLS results, for constructive discussion on self-assembly, and for generally putting up with me in the lab.

Finally I would like to thank my friends, family, and course mates, especially to the chem-phys lot, you have made my degree the most enjoyable it could be.

# Contents

|  |            |
|--|------------|
| <b>Abstract</b>  | <b>i</b>   |
| <b>Acknowledgements</b>  | <b>ii</b>  |
| <b>Contents</b>  | <b>iii</b> |
| <b>1 Introduction</b>  | <b>1</b>   |
| 1.1 The Energy Crisis . . . . .                                    | 1          |
| 1.2 Hydrogen Production . . . . .                                  | 2          |
| 1.2.1 Derivation from hydrocarbons . . . . .                       | 2          |
| 1.2.2 Electrolysis using centralised power . . . . .               | 2          |
| 1.2.3 Electrolysis by alternative energy introduction . . . . .    | 3          |
| 1.3 Diamond . . . . .  | 4          |
| 1.3.1 Bulk physical, chemical and optical properties . . . . .     | 4          |
| 1.3.2 Electronic properties and doping . . . . .                   | 5          |
| 1.4 Concepts for Diamond Electrodes . . . . .                      | 7          |
| 1.4.1 Doping . . . . .   | 7          |
| 1.4.2 Surface termination and negative electron affinity . . . . . | 8          |
| 1.4.3 Diamond-electrolyte interface . . . . .                      | 9          |
| 1.5 Electrochemical Water Splitting . . . . .                      | 12         |
| 1.5.1 Electrochemistry basic concepts . . . . .                    | 12         |
| 1.5.2 Photoelectrochemical water splitting . . . . .               | 13         |
| 1.5.3 Degenerate diamond electrodes . . . . .                      | 15         |
| 1.5.4 Surface states . . . . .                                     | 16         |
| 1.6 Motivation . . . . .   | 17         |
| 1.6.1 Previous photoelectrochemical research . . . . .             | 17         |
| 1.6.2 New materials for diamond electrodes . . . . .               | 18         |
| <b>2 Experimental</b>  | <b>20</b>  |
| 2.1 Materials . . . . .  | 20         |
| 2.2 Methods - Sample Fabrication . . . . .                         | 23         |
| 2.2.1 Dynamic light scattering . . . . .                           | 23         |
| 2.2.2 Polymer self-assembly . . . . .                              | 23         |
| 2.2.3 Ozone treatment and lithiation . . . . .                     | 25         |
| 2.2.4 Scanning electron microscopy . . . . .                       | 26         |
| 2.3 Methods - Electro/Photoelectrochemistry . . . . .              | 27         |

---

|          |   |           |
|----------|---|-----------|
| 2.3.1    | Electrochemistry instrumentation . . . . .  | 27        |
| 2.3.2    | Cyclic voltammetry . . . . .  | 29        |
| 2.3.3    | Chronoamperometry . . . . .   | 30        |
| 2.3.4    | Photocurrent-voltage spectra . . . . .  | 30        |
| 2.3.5    | IPCE-wavelength spectra . . . . .   | 31        |
| <b>3</b> | <b>Results and Discussion</b>   | <b>32</b> |
| 3.1      | Sample Fabrication Results . . . . .  | 32        |
| 3.1.1    | Dynamic light scattering . . . . .  | 32        |
| 3.1.2    | Microscopy results: self-assembly . . . . .   | 33        |
| 3.1.3    | Microscopy results: surface termination . . . . .   | 41        |
| 3.2      | Electro/Photoelectrochemistry results . . . . .   | 43        |
| 3.2.1    | Cyclic voltammetry and Xe lamp chronoamperometry in KCl . . . . .                             | 43        |
| 3.2.2    | Cyclic voltammetry and Xe lamp chronoamperometry in Na <sub>2</sub> SO <sub>3</sub> . . . . . | 46        |
| 3.2.3    | Cyclic voltammetry in EuCl <sub>3</sub> and Ar-Hg lamp chronoamperometry . . . . .            | 49        |
| 3.2.4    | Photocurrent-voltage spectra . . . . .  | 50        |
| 3.2.5    | IPCE-wavelength spectra . . . . .   | 55        |
| <b>4</b> | <b>Conclusion</b>   | <b>57</b> |
| 4.1      | Summary . . . . .   | 57        |
| 4.2      | Future Work . . . . .   | 58        |
|          | <b>Bibliography</b>   | <b>61</b> |
|          | <b>Appendix</b>   | <b>66</b> |

# Chapter 1

## Introduction

### 1.1 The Energy Crisis

The world's current energy problem is two-fold: (1) future consumption will be greater than we can currently produce, and (2) the production of energy is damaging the environment in an unsustainable way [1]. Current and future energy demands do and will take on different forms, for example the usage of an aircraft (powerful and decentralised) compared to a domestic household (connected centrally to the national grid). The need arises for a variety of green, abundant and economical energy media. At least one of these must be effectively and cheaply transported, as well as stored for consumption at times of low energy generation and high energy consumption.

One promising option for this portable, storable energy source is hydrogen [2]. Fuel cell technology is now able to output the same energy as petroleum powered engines if connected to an ideal (energy density) hydrogen storage vessel [3]. Hydrogen storage research may be slow, but it is making progress [4], and would be greatly stimulated by the advent of renewable, economical hydrogen production. Hydrogen can be produced in multiple ways. Significant methods include (1) derivation from hydrocarbons, (2) electrolysis of water using centralised power, (3) electrolysis by alternative energy introduction, *i.e.* novel technologies currently under development. Each of these approaches are discussed herein.

## 1.2 Hydrogen Production

### 1.2.1 Derivation from hydrocarbons

Current significant methods for hydrogen production include steam-methane reforming (SMR) and coal gasification, both of which use high temperatures and produce large amounts of carbon compounds [5]. While there may be ongoing attempts to increase the efficiency of these processes and the purity of their products, carbon oxides are inevitably produced in the reactions involved. Energy consumption is predicted to increase two-fold by the middle of the 21st century [6], and as it does, output of greenhouse gases will follow the same trend unless the carbon output per unit of energy is greatly reduced. This could only be realised through the use of hydrogen if SMR and similar methods are replaced by clean and renewable production techniques.

### 1.2.2 Electrolysis using centralised power

As a process which does not *directly* use non-renewable fuels or produce green-house gases, electrolysis is a favourable technique. For this reason its use in water splitting is experiencing an increase.

One practical hurdle for water electrolysis is the separation of evolved oxygen and hydrogen. The two products are highly reactive, so either they must be segregated immediately after production, or produced in a separated cell. The two prominent classes of electrolytic cell are outlined below.

#### Current Electrolysis Technologies

Solid oxide electrolysis cells (SOECs) use a layer of metal oxide to separate and mediate oxide ion flow between the two electrodes. They are essentially electrically reversed versions of commonly used fuel cells [7]. High temperatures cause the electrochemical kinetics and thermodynamics to improve significantly, radically increasing efficiencies [8]. However, this temperature requirement may mean use of SOECs is limited to industrial (and consistent) waste heat areas, such as existing power plants.

Conversely to SOECs, Proton Exchange Membrane (PEM) cells split the two halves of a cell via a polymer which allows  $H^+$  ion transfer [9]. Their low temperature operation allows decentralised use [10], and could provide storage of energy produced by small scale energy converters such as wind farms and solar cells in the future. That said, large scale production of renewable hydrogen would be implemented more easily if not impinging on current energy supply.

Unfortunately, only 19% of electrical energy is currently renewably sourced [11], which taints the electrolytic production of hydrogen with indirect carbon emissions. If electrolysis is going

to be viable in the long term, one of two things must happen: either vastly more centralised electrical energy must be renewably sourced, or the electrolysis process must be made renewable as a stand-alone technology, not drawing on central electrical power.

### 1.2.3 Electrolysis by alternative energy introduction

If the application of an external current was not a necessity for electrolysis then hydrogen production would be facile. This is the aim of much current research, four examples of which are: (1) Photocatalytic water splitting employing semiconductor nanoparticles [12], (2) Plasmon resonance enhanced water splitting employing metal nanostructures [13], (3) Photoelectrochemical (PEC) water splitting using semiconductor electrodes, and (4) High energy electron (beta) enhanced water splitting. Each of these techniques replaces the electrical power as the provider of energy to split water molecules.

The third and fourth of the above research interests are the focus of this report: the excitation of an electrode by radiation to induce the splitting of water.

This is by no means a young field of research. Fujishima and Honda made the first successful device that split water using only light in 1972 [14], which used a photo-anode of bulk  $\text{TiO}_2$  to oxidise water. This discovery also led to  $\text{TiO}_2$  and other materials being used in a wide range of photocatalytic applications [15–18], for example water purification. After more than 40 years since PEC water splitting was shown to be possible many issues still cause it to be economically impractical [19].

Water splitting by the excitation of an electrode by beta radiation has not yet been attempted. This project aims to ascertain the viability of this process. The excitation of wide band-gap semiconductors can cause high energy electrons to be available for electrochemical reductions. Specifically, lithiated diamond cathodes have many desirable properties which make them able to initiate useful reactions, such as proton reduction for hydrogen generation.

| Property                                | Value                | Units                |
|---|----------------------|----------------------|
| Sound velocity                          | $1.8 \times 10^4$    | m/s                  |
| Density                                 | 3.52                 | g/cm <sup>3</sup>    |
| Young's modulus                         | 1.22                 | GPa                  |
| Thermal expansion coefficient           | $1.1 \times 10^{-6}$ | K <sup>-1</sup>      |
| Thermal conductivity                    | 20.0                 | W/cm-K               |
| Optical index of refraction (at 591 nm) | 2.41                 | Dimensionless        |
| Electron mobility                       | 2200                 | cm <sup>2</sup> /V-s |
| Hole mobility                           | 1600                 | cm <sup>2</sup> /V-s |
| Bandgap                                 | 5.45                 | eV                   |
| Resistivity                             | $10^{13}-10^{16}$    | $\Omega$ -cm         |

TABLE 1.1: From ref [20]. Physical, optical and electronic properties of diamond.

## 1.3 Diamond

An expensive material in its natural state, diamond is an iconic gemstone known and coveted all over the world. It also has many unique physical and electronic properties which make it attractive for use in a wide range of technological applications. Although many of these uses are not yet realised, there are numerous areas of active research [21]. Table 1.1 shows selected properties of diamond, and this section outlines some notable and relevant characteristics.

### 1.3.1 Bulk physical, chemical and optical properties

Owing to its small atomic radius of 0.77 Å [22], carbon can form closely spaced lattice structures in diamond form. Its tetrahedral (sp<sup>3</sup>) arrangement of atoms, as shown in figure 1.1, causes some remarkable mechanical properties. For example the bulk modulus is well above 1000 GPa [23], making it vastly harder than other materials: steel has a modulus of around 160 GPa [24].

In addition to being the hardest known material, its tightly packed structure also gives diamond the highest thermal conductivity of any material, the fastest sound velocity, as well as a high degree of chemical inertness [27].

To date, numerous applications have utilised the impressive characteristics of diamond. Its hardness has enhanced the durability and strength of industrial tools, and its high thermal conductivity has found use in device heat dissipation [20].

Despite its extreme robustness, diamond is thermodynamically unstable. The free energy of the softer allotrope, graphite, lies 2.9 kJ mol<sup>-1</sup> below diamond under standard conditions [28]. For this reason, specialised techniques are required to synthesise the material. Chemical vapour deposition (CVD) [29], high pressure - high temperature (HPHT) synthesis [30], and detonation (explosion products) [31] are all used for different material requirements.

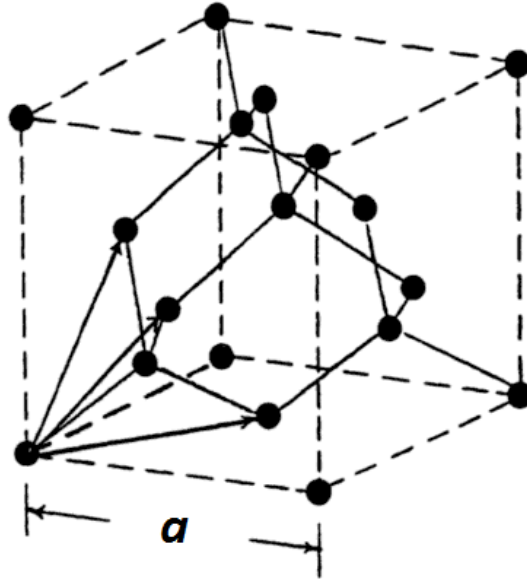


FIGURE 1.1: From ref [25]. The diamond unit cell. A carbon face-centred cubic (FCC) structure with a further carbon  $a(\frac{1}{4}, \frac{1}{4}, \frac{1}{4})$  from each existing atom, where  $a$  is a lattice vector equal to 3.567 Å [26]. Also shown by arrows are the three primitive vectors.

Diamond has a refractive index comparable to other semiconducting materials, equal to 2.41. This permits the use of diamond films in optical applications, such as lenses, where the large band-gap of 5.45 eV allows transmittance of a wide range of light wavelengths. The reflectance of diamond is 21% [32], which makes it usable in anti-reflective coatings for hard materials.

### 1.3.2 Electronic properties and doping

The electronic band gap of diamond is 5.45 eV [20], making it an insulator. However, its other properties have made diamond attractive for use in many electronic applications. Semi- and metallic conductivity can be achieved by doping (replacing carbon atoms) with elements such as boron, nitrogen and phosphorus. In the diamond bulk, these elements introduce electronic energy levels that lie within the band gap.

The p-type doping of diamond is well established and is achieved by doping with boron, an electron acceptor. The n-type doping of diamond is less facile, in part due the small size of the vacancy left by carbon atoms, meaning few elements can integrate into the lattice [33]. Additionally, difficulties arise from the high energy of the diamond conduction band [34]. Nitrogen is the most common electron donor in diamond, providing n-type doping. However, its energy level lies too far below the conduction band to give significant room temperature conductivity [33]. With phosphorus as the dopant, useful n-type diamond doping is becoming more easily achieved [35, 36].

Diamond has many other electronic characteristics which make it attractive. For example, it has a high breakdown field, saturation electron velocity, and electron mobility. When combined with its

---

hardness and thermal conductivity, these properties allow diamond to be used in electronics under extreme conditions, such as high temperatures [37].

One characteristic that makes diamond appealing for current research is its unmatched high energy conduction band [38]. This band position in principle makes it able to provide electrons with energies that are not attainable with most semiconductors. This can be made even higher by the use of specific atoms chemisorbed to the diamond surface, most commonly hydrogen. In a so-called “negative electron affinity” state, the conduction band electron energy becomes higher than that of a surrounding vacuum [39]. This effect finds uses in electron emission applications, and is widely researched. This and other properties of diamond electrodes are integral to the current project.

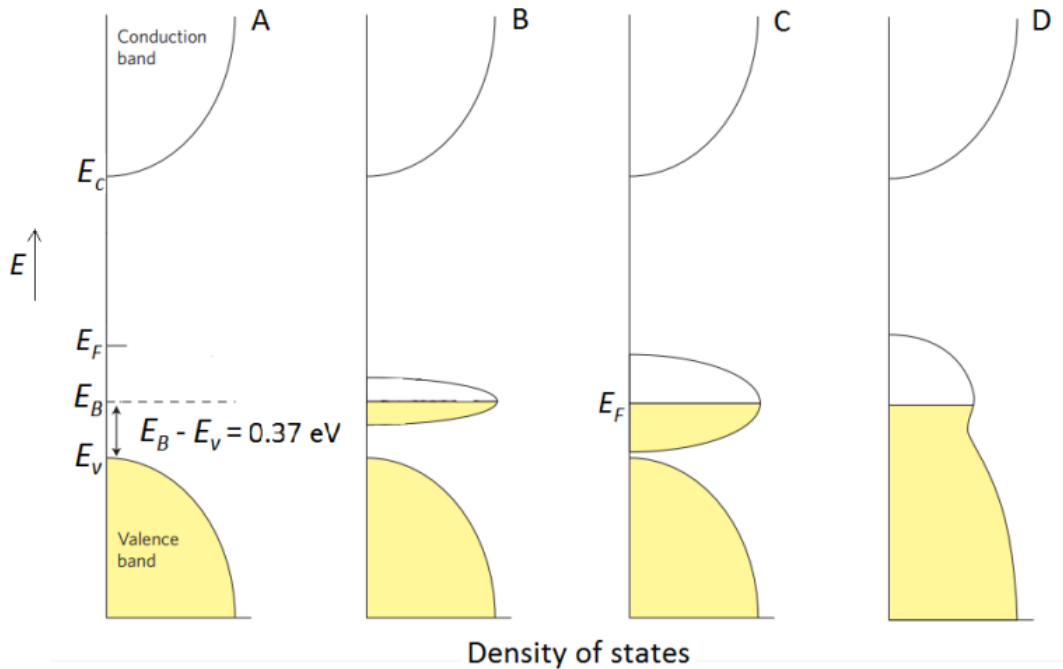


FIGURE 1.2: Adapted from reference: [40]. Schematic of the density of states as a function of energy in diamond at varied boron doping concentrations ( $T = 0$  K). As boron concentration increases (from **A** at weak doping levels to **D**, strongly doped) the energy level broadens, eventually causing a mixing of its states with the valence band, and thus inducing a continuum of energies around the Fermi-level. **D** is therefore a metallic state. Energy is shown vertically for comparison with similar schematics. Variables are defined in the main text.

## 1.4 Concepts for Diamond Electrodes

### 1.4.1 Doping

P-type doping is the primary method of rendering diamond conductive, and most commonly uses boron. As an atom with a similar covalent radius to carbon, it is easily introduced during CVD or by ion implantation with flow of, for example,  $B_2H_6$ . With one less electron per atomic site, boron introduces an empty energy level ( $E_B$ ) 0.37 eV above the valence band ( $E_v$ ) of diamond [25]. This allows electrons to be readily thermally promoted to the impurity level, leaving holes in the valence band. With such a small energy gap between  $E_v$  and  $E_B$ , the impurity level is near to maximally populated at room temperature. Figure 1.2 summarises the effects of boron doping on the bulk electronic structure. As shown, diamond can be doped at concentrations that turn it from an insulator into a semiconductor, and at high levels leave it a metallic conductor. Highly doped semiconductors in this metallic regime are termed *degenerate*.

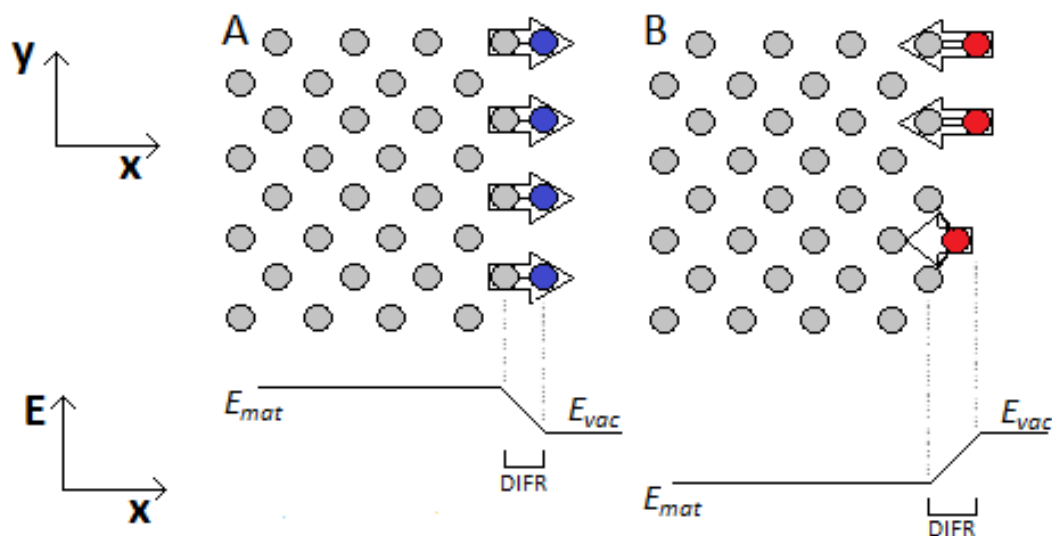


FIGURE 1.3: Schematic of surface dipoles caused by chemisorbed atoms on the diamond surface, using hydrogen (A, blue) and oxygen (B, red) as examples. The large arrows represent the dipoles, and the bonds made to the carbon (grey) atoms are shown by black lines. Oxygen can either bond to one or two carbon atoms as shown. The diamond tetrahedral bonds are omitted, and their orientation is not significant in this qualitative picture. Shown below each schematic are the relative energy of the vacuum ( $E_{vac}$ ) and material bulk ( $E_{mat}$ ) electrons. This shows how the dipole-induced field region (DIFR) alters the work function: by causing a field across the surface that electrons must move through.

#### 1.4.2 Surface termination and negative electron affinity

In the diamond bulk, carbon atoms have four other carbon atoms covalently bonded to them. By contrast, on the crystal surface the outward direction(s) have  $sp^3$  orbitals with only one electron in them, otherwise known as dangling bonds. In order to lower the energy of these energetic states, two things can happen, reconstruction and termination. Reconstruction can occur in the surface atoms, rearranging themselves into a new structure [41]. Important to diamond, termination is the bonding of surface atoms to other atoms and molecules. Examples of terminating species include hydrogen, oxygen and combinations including alkali metals [42]. Both termination and reconstruction can occur to stabilise the system, although they often have barriers to activation.

Surface chemisorbed atoms alter the electronic properties of the surface and therefore that of the bulk. This is due to the dipole, shown in figure 1.3, caused by the inherent charge imbalance across the carbon-surface atom boundary.

The work function ( $\phi$ ) is defined as the work required to remove an electron from the Fermi-level ( $E_F$ ) deep within the bulk of a material, move it through its chargeless surface and place it at infinity (not energetically affected by the material) [43]. Dipoles do not introduce any net charge to the surface, yet they do alter the energy required for an electron to be moved through it. As is shown in figure 1.3, the field induced by the dipole causes either a loss or gain of electron energy upon entering the material (or vice-versa upon leaving), dependent on dipole direction. This has

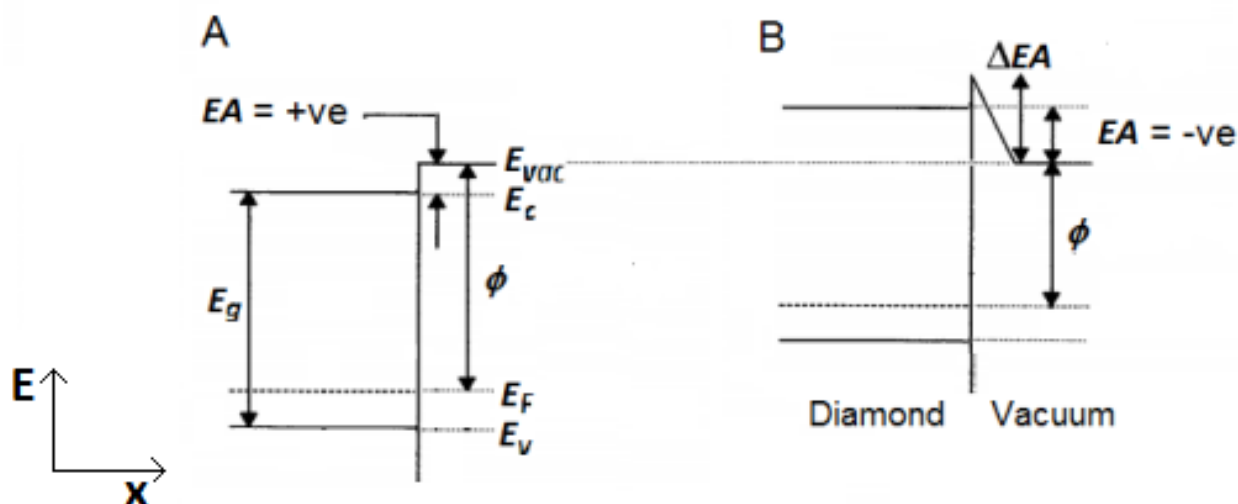


FIGURE 1.4: Adapted from reference: [44]. Schematic depicting the band energies at the clean (A) and H terminated (B) diamond surface. The work function ( $\phi$ ) and electron affinity ( $EA$ ) are shown relative to the vacuum electron energy ( $E_{vac}$ ), which is shown equal for both diagrams. Band bending (see section 1.4.3) at the surface is omitted for clarity.

the effect of shifting the band energy of the bulk diamond electrons up or down, raising or lowering their energy with respect to the vacuum.

For semiconductors, the electron affinity ( $EA$ ) is defined as the energy difference between the conduction band minimum ( $E_c$ ) and the vacuum level for electrons [45]. For most semiconductors  $EA$  has a large positive value. The extremely high  $E_c$  in diamond gives it such a small  $EA$  value, that when terminated with an outward dipole inducing species such as hydrogen, a negative  $EA$  value (NEA) is generated. This is depicted in figure 1.4, and implies that electrons in the conduction band of hydrogen terminated diamond can have greater energy than those in the vacuum [39].

### 1.4.3 Diamond-electrolyte interface

Due to the acceptor nature of boron in diamond, the Fermi-level is lower than that of the intrinsic material. For this reason, when p-type diamond makes contact with, for example, an electrolyte solution, electrons will flow in, across the interface. They will induce an electric field across the surface, this time caused not by a dipole but by built up charge. As shown in figure 1.5, this causes a shift in the bulk band energies. The surface band energies, however, are unchanged due to the lack of excess charge density there. The overall effect is termed “band bending”. Electrons, given enough energy (*i.e.* excited to the conduction band), will move to lower their energy and travel toward the surface. Equally, since their lowest energy state is upward on figure 1.5, holes in the valence band will move away from the surface into the bulk. Thus, a current is sustained in the electrode if holes are collected in the circuit and electrons induce a reaction at the surface.

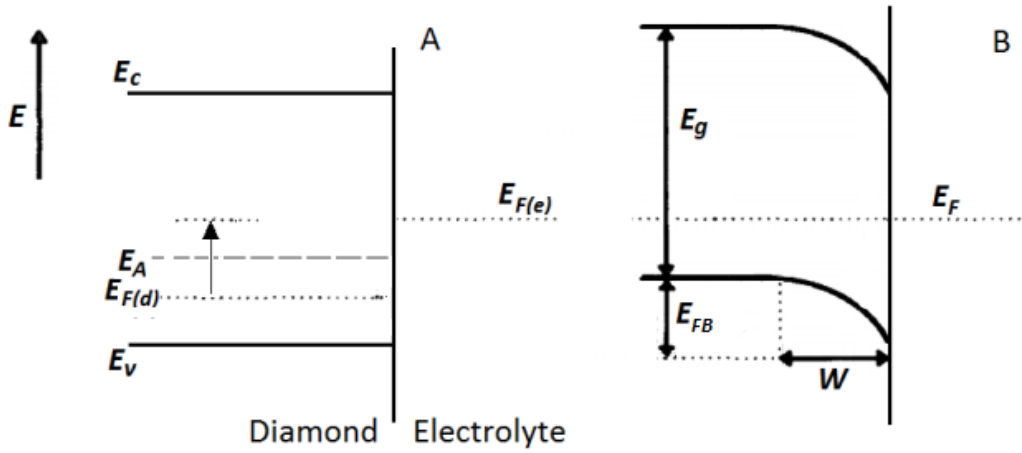


FIGURE 1.5: Schematic of diamond band energies near the diamond/electrolyte interface before (A) and at (B) equilibrium. Electrons flow across the interface, causing a charge imbalance and consequent electric field. This bends the bands up away from the surface into the bulk.

The magnitude of the band bending is known as the flat-band potential ( $E_{FB}$ ).  $E_{FB}$  is the applied potential required for the band-bending to be suppressed completely, and is dependent on the Fermi-level difference across the interface [46]:

$$E_{FB} = E_{F(e)} - E_{F(d)} \quad (1.1)$$

where the terms (see figure 1.5) refer to the Fermi-levels on each side of the interface, and [46]

$$E_{F(d)} = E_v + k_B T \ln \left( \frac{N_v}{N_A} \right) \quad (1.2)$$

in which  $N_v$  is the effective density of states in the valence band, a product of constants including the effective mass of holes, and  $N_A$  is the density of acceptor states when under complete ionisation. Equation 1.2 shows that as acceptor density increases, the Fermi-level drops logarithmically. Under high doping conditions, the Fermi-level tends towards the dopant level as shown in figure 1.2. This means that  $E_{FB}$  tends to a maximum. However, the distance over which the band bending takes place, the *space charge layer* thickness, is reduced [47]:

$$W = \left( \frac{2\epsilon E_{FB}}{eN_A} \right)^{1/2} \quad (1.3)$$

where  $e$  is the electronic charge and  $\epsilon$  is the relative permittivity of the diamond, 5.7 [20]. Equation 1.3 implies that as doping increases,  $W$  reduces with a square root dependence. At moderate doping levels,  $W$  would be on the order of a few nm, but once rendered degenerate at strong doping, it would be less than 1 nm.

Whatever the size and width of the band bending at the material surface, its combination with

---

the NEA should allow the conduction band at the diamond-electrolyte interface to act as a source of high energy electrons for reduction reactions. Based on this and other ideas outlined in the last three sections, NEA diamond should constitute an efficient cathode provided electrons can be excited at or near its surface.

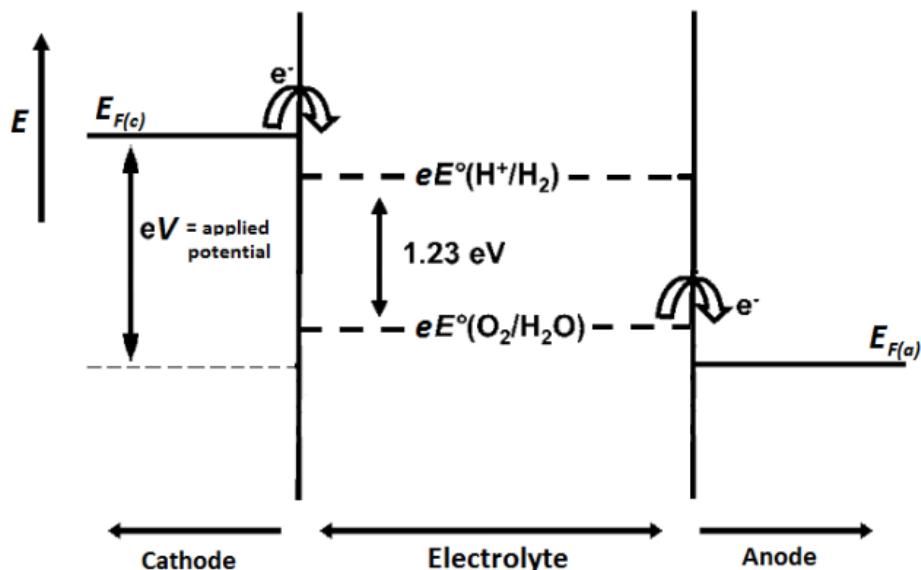


FIGURE 1.6: Adapted from ref [48]. Schematic of ideal electrolysis energy levels. The applied voltage causes the electronic energy levels of the electrodes to straddle the water redox potentials.  $E_{F(c)}$  and  $E_{F(a)}$  are the Fermi-levels of the cathode and anode respectively.

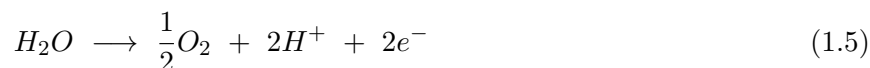
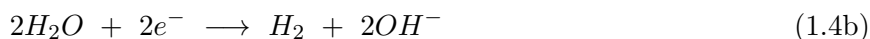
## 1.5 Electrochemical Water Splitting

Conceptually, electrochemical water splitting in its most basic form is electrolysis: the use of electrical current to drive the gas evolving reactions. As mentioned in section 1.2, photoelectrochemical water splitting is effectively electrolysis with an alternative introduction of energy. For this reason, before including concepts from the previous section, the ideas of electrolysis will be discussed.

### 1.5.1 Electrochemistry basic concepts

A potential difference is applied between two conducting electrodes submerged in water; one half of the process happens at each. This process is shown schematically in figure 1.6, depicting the relevant energies. The minimum voltage ( $E$ ) thermodynamically required to complete the process is 1.23 V, which gives 1.23 eV of energy per electron, and is shown between the individual redox potentials of the two half reactions.

Two electron transfer processes are shown in figure 1.6, which facilitate the reactions producing hydrogen and oxygen [49, 50]:



The cathodic reaction in acidic (1.4a) or in basic (1.4b) conditions is referred to as the hydrogen evolution reaction (HER). The anodic reaction (1.5) is named the oxygen evolution reaction (OER). The net reaction of the above processes (using either 1.4a or 1.4b) is:



In practice, the electrode potential difference for electrolysis of water is set between 1.6 and 2.0 V [51]. This is 0.4 – 0.8 V higher than the required potential for water splitting, a quantity referred to as the overpotential. Overpotential is an added potential required for activation of the reaction, transport of mass and overcoming resistance in the circuit, and can hinder a process even if enough voltage is applied thermodynamically. The overpotential is shown in figure 1.6 where  $E_{F(c)}$  and  $E_{F(a)}$  straddle the water redox potentials by a finite energy.

### 1.5.2 Photoelectrochemical water splitting

As boron-doped diamond (BDD) is a p-type material, electrons readily move through the space charge layer toward the surface (figure 1.5). This means it is most suitable for use as a cathode, initiating the HER. Using an NEA-BDD electrode and introducing photons into the electrochemical system yields the system studied in this project. Visualised another way, combining figures 1.5B and 1.6 and completing the circuit gives figure 1.7.

The introduction of energy in the form of light gives the above process enough energy to initiate reactions. If no bias is applied ( $E = 0$  V), the driving force then becomes  $E$  related to those outlined in section 1.4, namely the band bending and NEA of the diamond surface. Conduction band electrons at the NEA-BDD surface are poised to reduce species at the electrode/electrolyte interface. With this in mind, excitation of these electrons into the conduction band from the valence band is of greatest concern. As the band-gap ( $E_g$ ) of diamond is 5.45 eV, only light of wavelength shorter than 225 nm can achieve this (see also section 1.5.4).

Photocurrent is the current caused by separation of charges in the space charge layer and at the surface of the electrode. If the holes are collected and the electrons reduce a solvated species then the photocurrent is finite. Many photoelectrochemical concepts can be summarised by the Gartner equation for photocurrent density [53]:

$$j_{Ph} = eI_0 \left( 1 - \frac{\exp(-\alpha W)}{1 + \alpha L} \right) \quad (1.7)$$

where  $I_0$  is the incident photon flux density,  $\alpha$  is the absorption coefficient of the photoelectrode surface.  $L$  is the diffusion length of minority carriers, *i.e.* electrons:

$$L = (k_B T \mu \tau)^{1/2} \quad (1.8)$$

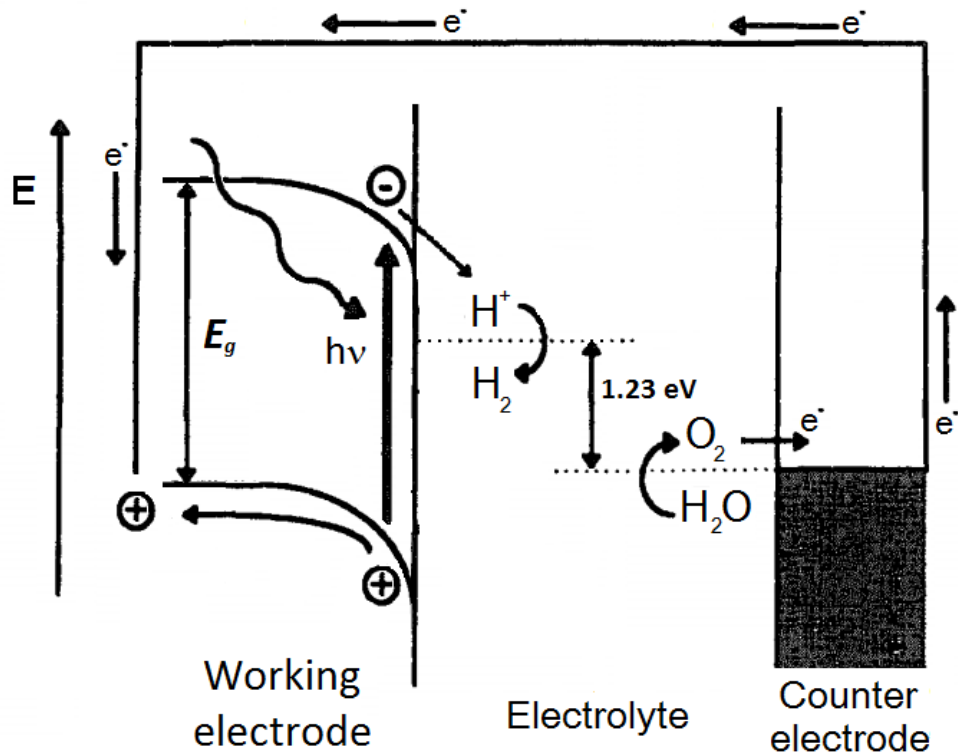


FIGURE 1.7: Adapted from reference: [52]. Schematic of a p-type photoelectrochemical water splitting device, such as the one examined here.

where  $\mu$  is the minority carrier mobility, and  $\tau$  is their lifetime.  $\mu$  in diamond is superior to those of other semiconductors [54], though it decays as doping increases [55]. However,  $\tau$  is only a few hundred ps, making  $L$  short in diamond. This means that only excitation near to the surface will cause separation of charges in the space charge layer, and subsequent photocurrent in the system.

Equation 1.7 shows that increasing  $L$  and  $W$  would increase the photocurrent produced by illumination. The diamond electrode can also be biased to alter the degree of band-bending. The thickness,  $W$  depends on  $E$ , the applied potential [53]:

$$W = W_0 E^{1/2} \quad (1.9)$$

where  $W_0$  is simply the layer thickness at  $E = 1$ . This introduces a bias dependence into equation 1.7. So the Gartner equation (1.7) predicts the increase in photocurrent when the electrode is biased, as shown in figure 1.8. This figure illustrates the power of the space charge layer and the charge transport characteristics to improve photoelectrochemical performance in semiconductor electrodes.

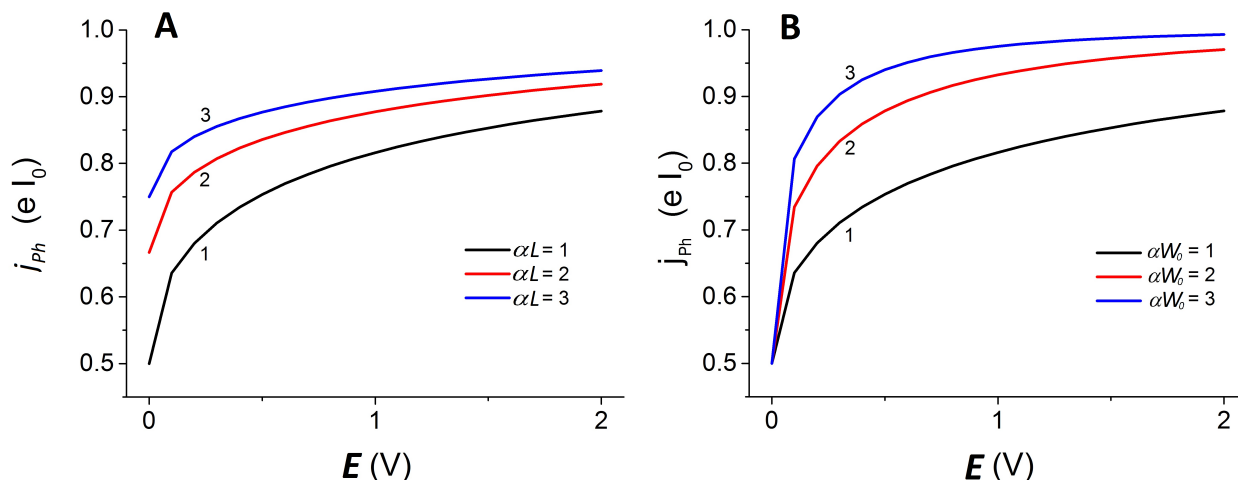


FIGURE 1.8: Theoretical plots of normalised photocurrent density as a function of applied potential,  $E$  for varying  $L$  (A) and  $W_0$  (B) according to the Gartner equation (1.7). In A  $\alpha W_0 = 1$  and in B  $\alpha L = 1$ . Lines are numbered relating to the respective legends. Both axes are a modulus so are shown positively.

### 1.5.3 Degenerate diamond electrodes

The above principles and the Gartner equation apply generally to non-degenerate semiconductors: those without strong doping, on the left side of figure 1.2. This regime of bulk band structure shifting with  $E$  is a case known as band-edge pinning. In this regime, charge builds up inside the semiconductor. A field is sustained within the material and the space charge layer is alterable; consequently the Helmholtz layer is constant with  $E$ .

On the other hand, degenerate diamond (DD) is affected very differently. Its Fermi-level lies within the valence band so it acts more like a metal, and is said to be Fermi-level pinned. The small size of the DD space charge layer means that potential differences between the bulk diamond and the electrolyte are sustained by the field in the Helmholtz layer, with a large charge build-up at the surface [56]. Hence as  $E$  is changed, the surface charge changes, and the field in the Helmholtz layer changes, which alters the Helmholtz potential  $E_H$ . This potential acts as a barrier to charge transfer across the interface, and can be lowered by reducing  $E$  [57].

Since the space charge layer is present only over a short distance in degenerate semiconductors, the incoming radiation may penetrate further than it into the material. This means that there is no electric field exerting a force on most excited charge carriers. Therefore, for deep excitations the only process allowing the separation of carriers and consequent current generation is their diffusion (or component of) in the relevant direction.

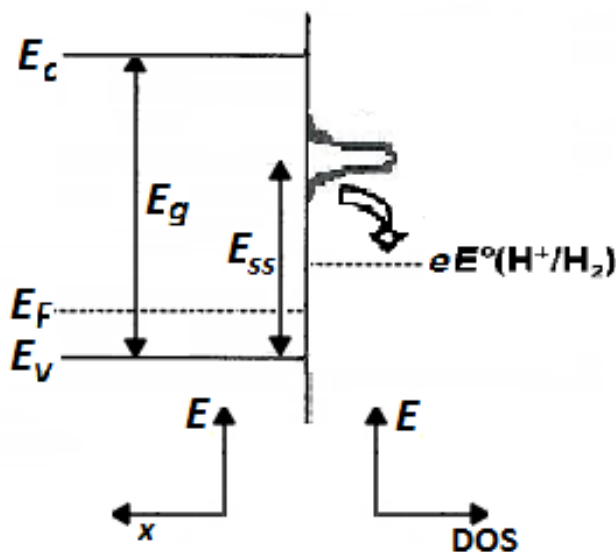


FIGURE 1.9: Schematic of density of surface states (DOS) on a diamond electrode surface. Band bending and other electronic effects are omitted for clarity. Illustrates how the surface states could facilitate reduction reactions (e.g. proton reduction) when excited by radiation of lower energy than  $E_g$ .

#### 1.5.4 Surface states

Generally caused by the same dangling bonds that chemisorbed species bond to, surface states are electronic energy levels that exist on the surface of a semiconductor. Their energies lie within the band-gap [58]. Related to the previous section, they can be degenerate with the Fermi-level, causing Fermi-level pinning.

As surface states are positioned within the band-gap, they can reduce the apparent band-gap of the material. They do this inasmuch as they will give a photo-response at lower incident photon energies than the band-gap would predict. This onset of photocurrent at low energies ( $E_{SS}$ ) could allow the reduction of hydrogen where it is generally unfeasible with diamond photocathodes. There is a considerable amount of research that has attributed photo-responses to surface states, as is discussed in the next section.

## 1.6 Motivation

The concepts in the previous sections give an overview of the relevant characteristics of diamond electrodes and their use in photoelectrochemistry. Following are examples of their use, as well as some further motivation for this project and the materials it uses.

### 1.6.1 Previous photoelectrochemical research

Due to its large band gap, diamond is not an inherently attractive material for commercial photoelectrochemical (solar) applications. The electro- and photoelectrochemistry of diamond have nevertheless been studied by various groups.

Pleskov *et al.* showed for the first time in 1987 that diamond could be used as a photoelectrode [59]. They used an undoped (yet p-type) CVD film to explore the semiconductor and surface properties of the material. Later, in 1991, boron-doped CVD diamond was studied by the group of Akira Fujishima [60]. This group showed that the higher p-type conductivity increased the photocurrent considerably. Both of these groups used sub-band gap illumination (xenon and mercury lamps) yet still observed photocurrents, attributing the effects to impurity and surface states inhabiting the band gap (and thus being populated under sub-band gap illumination). Electrodes also caused a change in solution pH when held at prolonged cathodic potentials and under illumination, suggesting that reduction of protons was occurring [60].

The above research was continued by Boonma *et al.* [61] to probe diamond electrodes with supra-band gap radiation. The group used excimer lasers of different energies: 6.4, 5.0 and 3.5 eV. The former gave an enormous photocurrent when compared to the 5 eV source, and the latter gave no photocurrent. This study indicated that valence to conduction band excitation in diamond can give photocurrents much larger than those of sub-band gap surface state excitations, and can also evolve hydrogen. In addition, the writers pointed to the power of conduction band electrons for initiating higher energy reduction reactions.

The work mentioned so far used hydrogen terminated diamond films. Rao *et al.* in 1999 [62] studied the effects of surface termination on electronic properties. This work showed that the oxygen and hydrogen terminated surfaces have different flat-band potentials ( $E_{FB}$ ). Values obtained have been ambiguous, but it is clear that oxygen termination shifts  $E_{FB}$  positively [63]. Also in 1999, Yagi *et al.* showed that decay of photocurrent in CVD films subjected to supra-band gap illumination is dependent on surface termination [64].

Some of the above early researchers in diamond photoelectrochemistry pondered the idea of electron ejection from the diamond surface [38, 61]. In principle this happens because the extreme high energy of the conduction band is higher in energy than that of solvated electrons. This recently led

two groups to examine photocatalytic reduction reactions on the diamond surface [65] and in the nearby solution [66].

In the first of the above studies, Myung Jang *et al.* showed hydrogen evolution, attributing it to surface catalytic reduction of protons [65]. Sub-band gap illumination was used. This study showed that H terminated particles had a greater photocatalytic activity than their O terminated counterparts. As with earlier work using sub-band gap light, the activity was attributed to surface states, which formed a “reservoir” of electrons on the H terminated material. The group proposed that the increased conduction band edge energy above the vacuum level caused the increase in activity, and the consequent disagreement with earlier work.

Zhu *et al.* used supra-band gap light from a Xe-Hg lamp to reduce  $N_2$  to ammonia [66]. Their work showed a far higher yield of ammonia with H-terminated than with O-terminated diamond particles. The group hypothesised that electrons were being ejected from the diamond into the surrounding electrolyte to induce  $N_2$  reduction. This can be attributed to the negative electron affinity; the inter-band excitation allows electrons to readily leave the material at high energy. Upon illumination, however, the negative electron affinity degraded over time, showing that hydrogen termination may not be stable enough to effectively carry out photoelectrochemical processes for prolonged periods. If the work of groups such as Rao *et al.* [62] is correct, then the NEA is in this work the main contributor to such high photocatalytic activity. For this reason, finding new more stable terminations for diamond may be highly productive for the field.

### 1.6.2 New materials for diamond electrodes

Much research into photoelectrode materials concerns ways to increase the interfacial surface area [67]. Established CVD techniques as well as deposition of HPHT particles tend to form thin films of low roughness factor (*real area/geometric area*). Films can therefore often have low surface area when compared to their nanostructured material counterparts.

Examples of solutions include Honda *et al.* who produced porous honeycomb structures in CVD diamond [68]. By using masked oxygen plasma treatment they were able to vastly increase the diamond/electrolyte interfacial area, multiplying the capacitance by 200 times. A group in Bristol, Zanin *et al.* made use of carbon nanotube (CNT) teepee structures to provide a porous scaffold for CVD diamond growth [69]. This improves the capacitance by 450 times relative to the flat thin film surface. In addition, the CNTs form a highly conductive link between the highly rough surface and the substrate. These approaches not only increase surface area for charge transfer, but also reduce the reflectivity of the electrode surface.

A problem experienced by studies on photo-reduction using NEA diamond has been the degradation of H termination under prolonged illumination [66]. Clearly stability of H on the diamond surface is

too low to withstand band-gap illumination for long periods. Many other terminations such as CeO are also weakly adsorbed to the surface [70]. Alkali metal-oxygen terminations do provide large NEA values, however, so T.L. Martin and his group at Bristol employed a lithium coating on an O terminated diamond surface [71]. This OLi terminated surface was tightly bound: calculated 4.4 - 4.7 eV depending on orientation. It also gave a strong NEA: calculated -4.0 - -4.5 eV, and observed -2.1 eV. Hydrogen also has a strong binding energy on diamond surfaces, for example on the (100) surface it can be 5.4 eV or more [72]. However, experimentally, the NEA for H terminated surfaces is around -1.3 eV [73], providing a lower driving force for electron ejection from the surface. Further research is needed to ascertain how the NEA properties of diamond terminations translate into properties of their photoelectrochemical systems.

Diamond is well known to have a notably high radiation hardness [74]. This means it is resistant to the destructive capabilities of ionising radiation that tend to degrade many materials. However, in absorbing ionising radiation, diamond can have many electrons excited within it. Just as photons with energy  $> E_g$  excite electrons, beta radiation (for example) can excite electrons to the conduction band, but with many times the quantity per incoming particle. The effect finds use in radiation detectors [75], but could potentially be used as a source of conduction band electrons without the need for high energy photons. Whole cells for this purpose must be radiation resistant, but if a suitable one is constructed, this could provide a method of consistent water splitting without carbon emissions.

In order to produce electrodes with desirable characteristics for water splitting applications, the first part of this project concerns optimisation of an electrode fabrication process. This optimised electrode could find applications in beta-enhanced, as well as photoelectrochemical water splitting. This can then be compared to porous CVD diamond electrodes, with a selection of terminations to gauge the characteristics of the materials. By comparison of the photoelectrochemical activity and properties of different surface terminations, the viability of conducting NEA diamond for proton reduction will be established.

## Chapter 2

# Experimental

### 2.1 Materials

All diamond used in this project was boron-doped. Material was produced either by HPHT synthesis for the self-assembly process (see section 2.2.2), or by CVD and kindly donated by Dr H. Zanin.

The HPHT diamond (Element Six) was received in the form of free-standing polycrystalline (consisting of 200  $\mu\text{m}$  polycrystals) boron doped diamond, in squares of 10x10x1 mm. Boron doping in these samples was of the order of  $10^{21}$  B atoms  $\text{cm}^{-3}$ . The samples were ball milled (Retsch, MM200) with steel ball bearings at a rate of 20 Hz for 7 hours, then with latex bearings at the same rate for 3 hours in order to reduce the crystal size. The resulting powder was then acid treated by Dr. Neil Fox, who heated the sample in  $\text{H}_2\text{SO}_4$  (95%, Aldrich). Once heated above 100  $^\circ\text{C}$ ,  $\text{KNO}_3$  (70%, Aldrich) was added in a mass per volume percentage of 6.5%, then heating continued to 200  $^\circ\text{C}$ , where the combination was held under reflux for 5 hours. Consequently, the sample was oxygen terminated. Suspension in an aqueous solution containing a phosphate buffer ( $\text{NaOH}/\text{KH}_2\text{PO}_4$ , 0.1 mol  $\text{dm}^{-3}$  each, pH 8.1) negatively charged the surface oxygen. Polyethyleneimine (PEI, Aldrich, see 2.2.2 for  $M_W$ ) and 3-Mercaptopropionic acid (MPA, 99%, Aldrich), a thiol, were used in self assembly and are shown in figure 2.1. Section 2.2 details the method for producing BDD electrodes with structure as shown in figure 2.2.

The as-grown CVD diamond samples were H terminated. A complete description of the sample preparation is given by Zanin *et al.* [69, 76]. In summary, aligned CNTs were grown onto titanium substrates by microwave CVD. These CNTs were electro-sprayed with a detonation nanodiamond suspension in methanol, causing clumping of the CNT tips to form teepee structures. The nanodiamond then served as seeds for diamond growth in a hot filament CVD reactor (1.5 hr, 1%  $\text{CH}_4/\text{H}_2$ , with  $\text{B}_2\text{H}_6$ ). This gave a 500 nm thick polycrystalline diamond film, with the boron doping concentration dependent on  $\text{B}_2\text{H}_6$  flow rate. The rates used for samples here were 0.1 and 0.2 sccm,

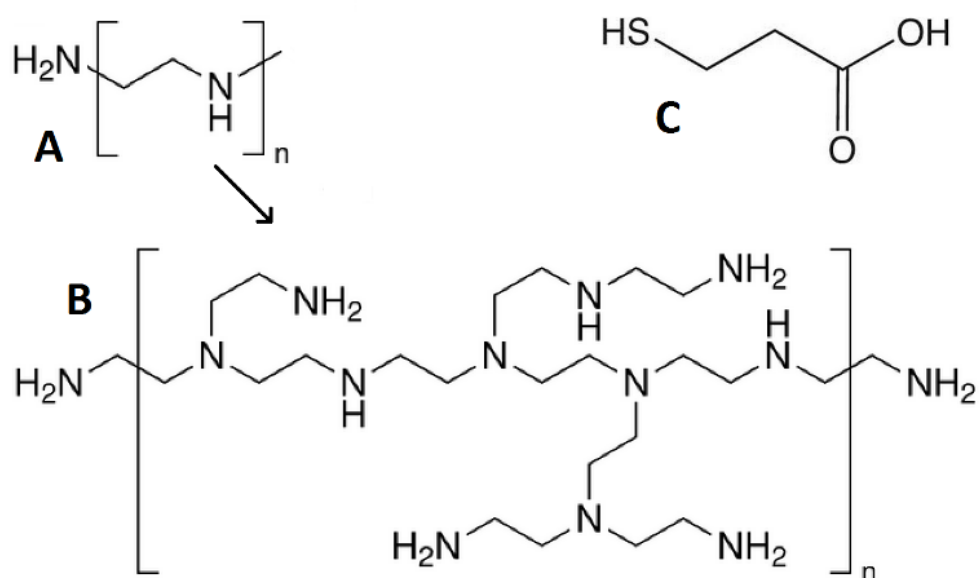


FIGURE 2.1: Structures of PEI and MPA. **A** is the monomer unit,  $\text{CH}_2\text{CH}_2\text{NH}$ , and **B** shows examples of branching, which is common to PEI. When solvated, PEI is protonated and provides of positive charge. **C** shows the structure of MPA, which when solvated deprotonates to provide a negative charge.

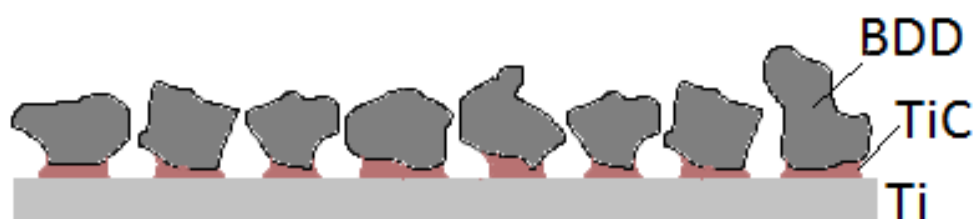


FIGURE 2.2: Schematic cross-section of titanium/titanium carbide/diamond structure. TiC is here used as an ohmic contact that binds the BDD to the Ti surface. Schematic is not to scale.

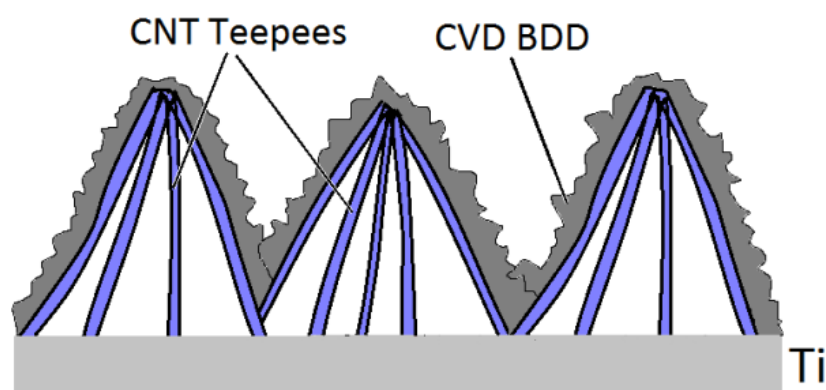


FIGURE 2.3: Schematic cross-section of titanium/CNT/diamond structure. The BDD is dark grey, CNTs are blue, and Ti is light grey. CNTs per teepee is greater in actual samples, and schematic is not to scale.

---

both doping the material to between  $10^{20}$  and  $10^{21}$  B atoms  $\text{cm}^{-3}$ , and referred to hereafter as 0.1H and 0.2H respectively. Figure 2.3 shows a schematic of the sample structure. As received, these samples were ready to be used in the techniques outlined in section 2.3. They were however also examined in the scanning electron microscope as defined in section 2.2.4.

## 2.2 Methods - Sample Fabrication

Here the sample fabrication method is summarised, before each section is outlined in more depth and details are given.

The ball-milled and acid treated basic diamond suspensions were drop cast onto PEI (or MPA + PEI) coated Ti substrates. After solvent evaporation and diamond deposition had occurred, the samples were vacuum annealed. Ozone treatment then consolidated the oxygen termination on the diamond surface, before evaporation coating of lithium.

### 2.2.1 Dynamic light scattering

Dynamic light scattering (DLS) is a method used to identify the sizes of small particles in suspension. To do this, a monochromatic light illuminates a sample, and the Rayleigh scattered light is measured. The frequency of changes between constructive to destructive interference is related to the Brownian oscillation rate and therefore to particle size. Small particles move more quickly than larger ones, so the output signal will have a higher frequency.

DLS was carried out in order to obtain the size distribution of diamond particles. Results were taken at three stages of the sample preparation process: after ball-milling, after acid treatment, and after centrifugation for 30s (see section 2.2.2).

#### Method

Results were taken (on a Malvern NanoS90 Zetasizer) in sets of 12 measurements, repeated 9 times. Each repeat took approximately 3 minutes. To ensure that minimal aggregation had occurred over the measurement time, the sample was sonicated before each set of 3 repeats, for a total of 3 times per sample. One plot per repeat measurement is given in the results, plotted on a set of axes for each stage of preparation. Centrifugation used a Labnet International portable centrifuge.

### 2.2.2 Polymer self-assembly

For effective photoelectrode production, the optimum characteristics must be considered. Here, the optima consist of a high (or complete) surface coverage of diamond, and a thin layer of particles on the Ti surface. Satisfaction of both of these allows a large surface area for light absorption and electron transfer, as well as a short distance for charge carriers to travel, minimising resistive effects on the efficiency through defect scattering.

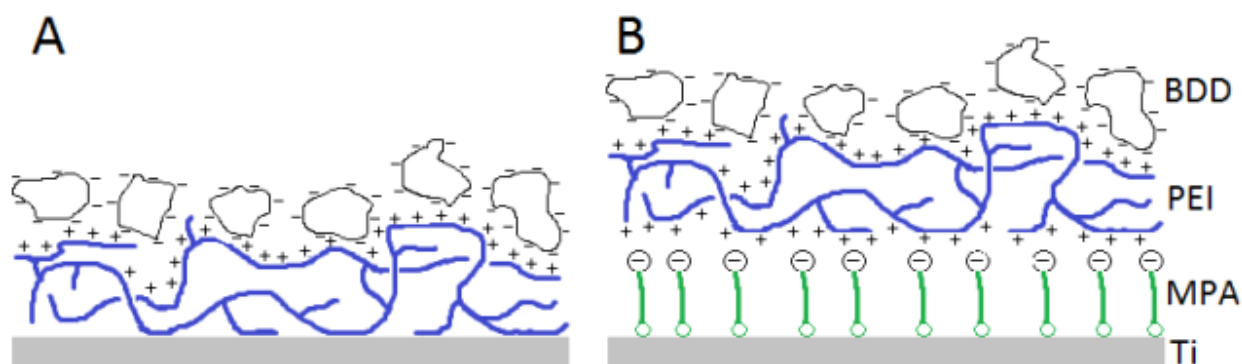


FIGURE 2.4: Schematic cross section of PEI (**A**) and MPA+PEI (**B**) self-assembled samples. PEI adsorbs to the Ti surface. Positive charges on the protonated PEI are attracted to the negative surface oxygen on the diamond. MPA thiol is negatively charged at one end, so in **B** it attracts the PEI more strongly. The MPA binds well to the Ti substrate, so adheres the PEI to the Ti more strongly overall. Schematic is not to scale.

Tailoring the self-assembly process to achieve these optima requires fine tuning of various parameters, table 2.1 shows those studied here. Prior to this is a description of the method, with numerical details for the tuned parameters omitted: instead they are marked with an asterisk (\*).

## Method

Titanium substrates (10 x 10 x 0.5 mm, >99%, Aldrich) were sequentially sonicated in Milli-Q water (18 M $\Omega$ , Millipore Milli-Q system), acetone, ethanol and methanol for 10 minutes each. They were dried under flow of nitrogen after each solvent. Submergence in a 1 mmol dm<sup>-3</sup> ethanolic solution of MPA\* overnight allowed the thiol to form a self-assembled monolayer on the substrate surface [77]. Rinsing briefly with ethanol followed by Milli-Q water removed any excess thiol. The substrates were then submerged in PEI solution\* for 1 hr, allowing it to adsorb to the substrate surface. Brief rinsing with Milli-Q water removed the excess polymer. After sonication, the diamond suspension\* was drop cast onto the substrates and left to deposit and evaporate, ensuring the smallest particles had deposited. See figure 2.4 for a schematic of the resulting sample. Finally, brief rinsing with Milli-Q water removed excess diamond, before vacuum annealing\* (Balzers 510 coating machine) to remove the organics and form a titanium carbide layer between the substrate and diamond. This left a thin layer of diamond chemically bound to the substrate as in figure 2.2.

## Optimisation parameters

| Process            | Parameter       | Options/range                | Units                  |
|--------------------|-----------------|------------------------------|------------------------|
| MPA thiol          | Use             | Yes/no                       | –                      |
| PEI solution       | m/v             | 0.05 – 0.1                   | g dm <sup>-3</sup> /10 |
| PEI solution       | Polymer $M_w$   | 1200 – 800,000               | g mol <sup>-1</sup>    |
| Diamond suspension | Sonication time | 1.5 - 6                      | hours                  |
| Diamond suspension | m/v             | 0.1 – 0.5                    | g dm <sup>-3</sup> /10 |
| Diamond suspension | Treatment       | Shaken/top layer/centrifuged | –                      |
| Annealing          | Temp. / time    | 700 / 30 – 1000+ / 90        | °C / s                 |

TABLE 2.1: Sample fabrication optimisation parameters. Each of the four processes refers to an asterisk in the Method section. Centrifugation (Labnet International) was for 30s. m/v stands for mass per volume, used for weighed substances suspended/solvated in liquid.

**Notes.** Use of m/v units for polymer concentration was important due to the vast difference in the molecular weight of each polymer. “Shaken” refers to physical shaking of the suspension vial to incorporate all sedimented diamond. “Top layer” refers to simply extracting the highest point of liquid in the diamond suspension, to take the smallest particles. Annealing was in each case carried out at a base pressure of  $5 \times 10^{-5}$  Torr ( $6.7 \times 10^{-3}$  Pa).

### 2.2.3 Ozone treatment and lithiation

In order to consolidate the oxygen termination on the diamond surface, the samples were ozone treated. During this process, UV light (254 nm) illuminates the samples while under flow of ozone ( $O_3$ ). The surface states (dangling bonds) of diamond become highly reactive and are easily oxidised by the ozone, causing a very high coverage of O atoms chemisorbed to the surface.

Samples were lithiated in order to produce an OLi termination on the surface, create an outward pointing dipole (figure 1.3A), and induce an NEA. High temperature lithium evaporation caused thin layer deposition of lithium onto the sample, where it was able to react with the terminating oxygen to form OLi on the surface. Samples with oxygen and oxygen-lithium termination will hereafter be referred to using O and OLi.

## Method

Samples were placed in the ozone cleaner (Jelight UVO 42A-220), which ran for 1 hour.

Dr. Neil Fox carried out the lithiation using the Balzers 510 coating machine, in which a lithium sample was heated (900 °C) in a tungsten dimple boat source under low pressure ( $5 \times 10^{-5}$  Torr),

30 cm from the diamond sample. A thin layer of lithium was then formed at  $0.3 \text{ nm s}^{-1}$  for 100 s, which once cooled and in air, was rinsed in Milli-Q water and dried, leaving just chemically bound lithium.

#### **2.2.4 Scanning electron microscopy**

Scanning electron microscopy (SEM) is a commonly used high resolution, high magnification microscopy technique. It illuminates a sample with high energy electrons via electron optics (magnetic and electric fields). These electrons then partially scatter away from the surface of the material, and can be detected much like light in an optical microscope. As long as a sample is conducting (or coated in a conductor), and is stable under high vacuum, it can be imaged at a higher magnification than almost any other technique. SEM was used to gain estimates of surface coverage and layer thickness, in order to tune the self-assembly parameters.

#### **Method**

SEM images were taken with a field emission gun (FEG) JEOL JSM-6330F microscope and a tungsten filament JEOL JSM-5600LV microscope. Surface coverages were estimated by imaging at various magnifications, but always comparing equal magnifications. Samples imaged were those produced in the previous two sections, as well as the 0.1H and 0.2H samples.

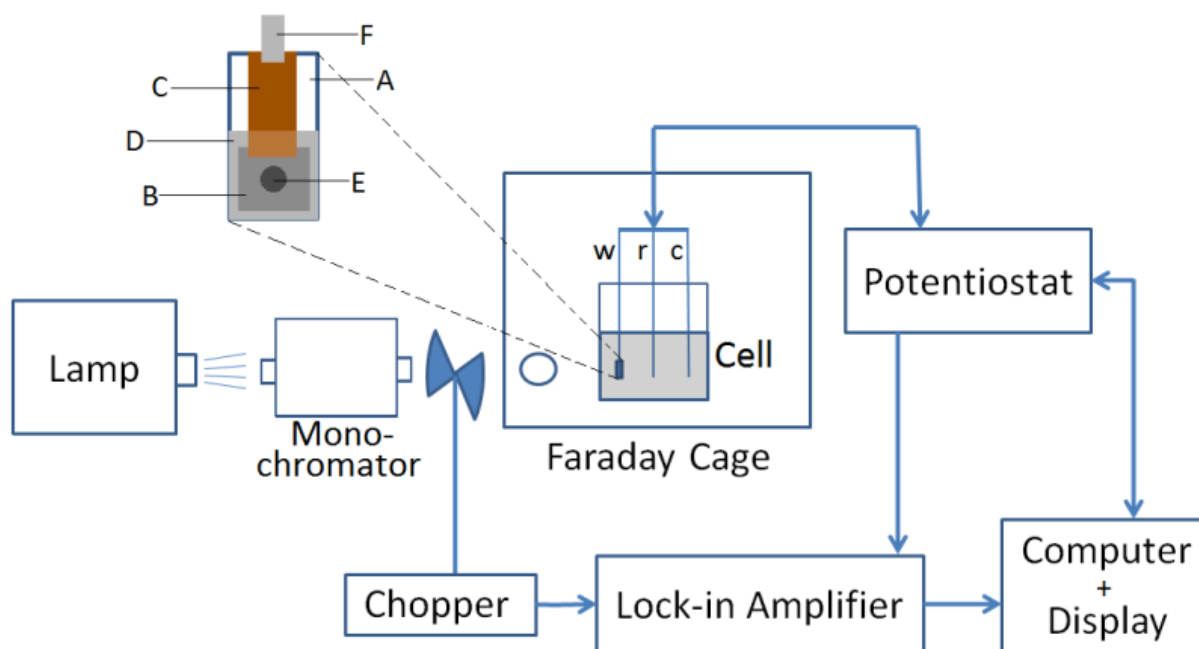


FIGURE 2.5: Schematic showing the physical set-up of electronics, as well as electrodes. These are the working (w, diamond electrode, shown expanded), the reference (r, Ag/AgCl), and the counter (c, Pt) electrodes. The cell contains the electrolyte and houses all electrodes. The named instruments are introduced in the main text, as are the lettered components of the working electrode.

## 2.3 Methods - Electro/Photoelectrochemistry

In order to explore the properties of self-assembled thin films of NEA-BDD, they were tested in aqueous electrochemical environments. This not only provides the necessary protons for reduction to produce hydrogen, but also a medium to which different electrolytes can be introduced. Electrolytes carry charge in solution and therefore facilitate the flow of current through the solution. Charge lost or gained at one electrode is regained/lost at the opposing electrode. This allows the unhindered probing of current while altering the voltage (with respect to a reference electrode), or over time. Section 2.3.1 describes the electrodes, electrolytes and electronics for the experiments in the following sections.

### 2.3.1 Electrochemistry instrumentation

The main components of the set-up used for electro- and photoelectrochemistry are shown in figure 2.5. This includes all components necessary for the range of measurements in the following sections. This section firstly describes the role of each electronic component in the set-up, before briefly illustrating the working electrode assembly method.

**Cell.** Houses the electrolyte solution, either KCl, Na<sub>2</sub>SO<sub>3</sub> or EuCl<sub>3</sub>. Houses the three electrodes, the diamond working/photo- electrode, an Ag/AgCl reference electrode (to provide a known reaction

potential for the applied potential to be measured against) and a Pt counter electrode (to complete the circuit and for current measurement). It is made from glass, with a quartz window to allow short wavelength light to propagate into the cell and illuminate the working electrode.

**Potentiostat (Ivium Compactstat).** With input from the computer user interface, controls the potential of the working electrode with respect to the counter, measured against the reference. Also measures current, which can be measured over time.

**Computer + Display.** Runs the user interface for the potentiostat and lock-in amplifier (Iviumsoft, Vivid). Inputs variables and outputs raw data.

**Lamps.** Illuminate the sample. Two lamps were used in this project, the first one being a xenon arc lamp (bulb: 150 W, Newport 6255). This lamp outputs a wide range of energies (a spectrum can be seen in the appendix) that are entirely below the band-gap of diamond. The second lamp used was a discharge tube containing argon and mercury at low pressure, kindly donated by John Rowden. This lamp has a less broad spectrum (that can also be found in the appendix), but may also output wavelengths shorter than those required to excite across  $E_g$ . This could not be ascertained in this project, as these wavelengths were not detectable by the UV-Vis spectrometer (Avantes avaspec 2048). However, the distinct smell of ozone does suggest that it was producing supra-band gap radiation. Due to the low path length of this type of radiation in air (absorption by  $O_2$ ) this lamp was used in very close proximity to the cell ( $\simeq 3$  cm from the working electrode) inside the Faraday cage.

**Monochromator (GM252).** A mechanical instrument that diffracts light into narrow wavelength bands, redirects the light using mirrors and outputs only the narrow band in its original direction. Wavelength is changed manually. The spectrum of an example wavelength can be found in the appendix.

**Chopper (Scitech).** A spinning disk, 50% opaque, modulates the light input to the cell. Frequency used was  $1.3 \pm 0.1$  Hz.

**Lock-in Amplifier (Stanford Research SR830 DSP).** Receives input from the chopper and from the potentiostat. Chopper inputs a square wave (on/off) and potentiostat inputs current, an oscillating signal due to the modulated light. Compares the current signal to the square wave of light. The magnitude of increased current that is in-phase with the square wave is output as the *real* current, and that which is out-of-phase is output as *imaginary* current. These signals frequently require rotation in the imaginary plane, as the phase of the chopper is relative, and the instrument may place the two input signals at the wrong relative phase (see section 2.3.4).

**Working electrode assembly.** The inset in figure 2.5 has letters in chronological order of assembly, *i.e.* **A** is the first component, and **F** is last. **A** is a glass slide; **B** is the sample, adhered to **A** by conducting silver paint; **C** is conducting copper tape, which makes direct contact with the sample

as well as via silver paint; **D** is inert Teflon tape, sealing the electrolyte solution away from the sample/copper tape; **E** is a circular hole in the Teflon tape where the sample is exposed,  $0.071 \text{ cm}^2$ ; **F** is a crocodile clip, making contact with the potentiostat input/output.

### 2.3.2 Cyclic voltammetry

Cyclic voltammetry (CV) is a dark (no illumination) method of probing the characteristics of a system over a range of potentials. Here it was used to find potential windows (a range of potentials) in which the electrode was both stable, and was initiating no electrochemical reactions purely through its applied voltage.

In a CV measurement, the potential of an electrochemical system (as described above) is scanned from one potential to another and back, linearly in time. Figure 2.6 shows this scanning process. The current is measured as a function of the potential. At large positive potentials the current will increase rapidly; at large negative potentials, the same will happen but with negative sign. This is due to the potential being great enough to induce oxidations and reductions such as the OER and HER. However, for photoelectrochemistry, it is best to exclude these processes so that the photo-induced processes can be detected. For this reason, CVs provide useful knowledge on the central section, giving potential windows for photoelectrochemical measurements.

#### Method

Each sample, 0.1H, 0.2H, O and OLi were tested by CV measurements. They were scanned whilst submerged in three different electrolyte solutions. KCl was used as an inert electrolyte, able to carry charge from one electrode to another.  $\text{Na}_2\text{SO}_3$  was used as a hole scavenger (it is easily oxidised) to facilitate positive current, and  $\text{EuCl}_3$  was used as an electron scavenger (it is easily reduced) to facilitate negative current. Measurements were taken at  $-0.6 < E < 0.2 \text{ V vs. Ag/AgCl}$ , in  $\text{Na}_2\text{SO}_3$ , at  $-0.2 < E < 0.6 \text{ V vs. Ag/AgCl}$ , in KCl and at  $-0.4 < E < 0.5 \text{ V vs. Ag/AgCl}$  in  $\text{EuCl}_3$ . CV measurements were taken at  $50 \text{ mV s}^{-1}$ .

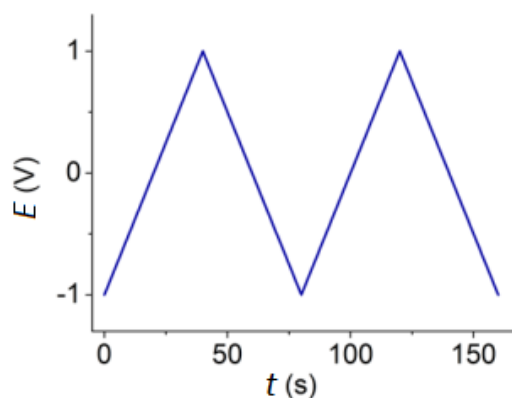


FIGURE 2.6: Potential as a function of time in a CV measurement, 2 cycles at  $50 \text{ mV s}^{-1}$ , arbitrarily between -1 and 1 V.

### 2.3.3 Chronoamperometry

Chronoamperometry is a measurement in which the potentiostat holds the potential difference at a constant value, over a specified time period. This can be used to probe the transient characteristics of a system. For example, in this project this technique measured the difference in current prior to illumination with the current during illumination. This gave plots of how the photocurrent evolved with time after switching on the light source.

#### Method

For each sample/electrolyte combination, the potentiostat held  $E$  constant and the current was allowed to stabilise over time. After stabilisation the sample was illuminated and the resulting current change was plotted as photocurrent. By rotating the chopper by 90 degrees, the illumination could be simply switched on/off. Measurements used illumination from either the Xe arc or Ar-Hg discharge lamp.

### 2.3.4 Photocurrent-voltage spectra

Photocurrent-voltage spectra use the potentiostat to hold the potential constant for a short time, while the chopper modulates the light. The lock-in amplifier outputs the real and imaginary current as described earlier. Measurement at a range of potentials produces a spectrum of photocurrent as a function of voltage.

#### Method

Using a Lab-view altered version of the Ivium software (VIVID), a potential range was specified for specific sample/electrolyte combinations based on CV results. This program controlled the process and converted raw data to output current results. Chopper frequency was specified as accurately as possible and was  $1.3 \pm 0.1$  Hz. These measurements could be carried out accurately with the O and OLi samples. Whereas the 0.1H and 0.2H samples produced spectra with a high degree of noise and little reproducibility, likely due to poor connections. To account for inaccuracy in the chopper-photocurrent phase correction, the real and imaginary parts of the photocurrent spectra needed rotation in the real-imaginary plane. This required use of the following rotation matrix:

$$\begin{pmatrix} I_r \\ I_i \end{pmatrix} = \begin{pmatrix} \cos(\theta) & -\sin(\theta) \\ \sin(\theta) & \cos(\theta) \end{pmatrix} \begin{pmatrix} I_{r0} \\ I_{i0} \end{pmatrix} \quad (2.1)$$

where  $\theta$  is the phase correction in radians,  $I_{r0}$  and  $I_{i0}$  are the original real and imaginary parts of the photocurrent respectively, and  $I_r$  and  $I_i$  are their corrected values. The implementation of this

correction is discussed in the results section. The Ar-Hg lamp was used for photocurrent-voltage measurements.

### 2.3.5 IPCE-wavelength spectra

IPCE (Incident photon to current conversion efficiency)-wavelength spectra can be used to show the response of the system to a range of wavelengths. This is important to ascertain the energy of electronic transitions producing photocurrent, as well as evaluating a cell for practical use. Wavelengths are specified by the monochromator and photocurrent is measured for each. IPCE can be calculated by [78]:

$$IPCE (\%) = 124000 \times \frac{j_{Ph}}{\lambda_{nm}(P_i/A)} \quad (2.2)$$

where the numerical prefactor has units of  $\text{J m C}^{-1}$ ,  $j_{Ph}$  is photocurrent density as in the Gartner equation (1.7),  $\lambda_{nm}$  is the wavelength in nm, and  $P_i/A$  is the incident power density from the illumination.

### Method

Using the same process described in section 2.3.3, chronoamperometry was used to measure photocurrent of O and OLi samples at wavelengths between 250 and 470 nm. A specified potential gave a constant background current, from which photocurrent could be measured at monochromated wavelengths every 10 nm. The monochromator provided a narrow peak width from the Xe arc lamp, an example of which is shown in the appendix. This was unfortunately unachievable with the 0.1H and 0.2H samples due to an unexpectedly high background current (see section 2.3.4 above), which inhibited the detection of very small photocurrents.

## Chapter 3

# Results and Discussion

### 3.1 Sample Fabrication Results

#### 3.1.1 Dynamic light scattering

Taken at three stages of the preparation process, the DLS show a general decrease in the size with each procedure, as shown in figure 3.1.

During the acid treatment process, harsh acidic and heating conditions effectively strip away diamond atomic layers. After the 5 hour period, this leaves a faceted crystal: one whose surfaces are predominantly the most stable crystal planes. In diamond, these are in general the (100), (110) and (111) planes of the face-centred cubic structure (figure 1.1) [79]. This stripping of layers is responsible for the decrease in size, which agrees with the two distributions shown. The total range of sizes has changed only by a factor of 2 at most, but the bulk of the sample has reduced more considerably (after acid treatment the plot is skewed more toward smaller sizes). This implies that the smallest and largest particles have not lost as considerable a portion of their size as those of average size. Those of initially extreme sizes are potentially already faceted, stable particles that have retained their size through much of the preparation process.

The centrifugation step, as expected, does not lower the range of particle sizes. It does however, limit it somewhat to the smaller regime. The increased effect of gravity (making larger particles sediment) forces only small particles to suspend well in aqueous environments. Assuming no aggregation, it is clear then that the centrifuge method is effective in providing a small particle size distribution.

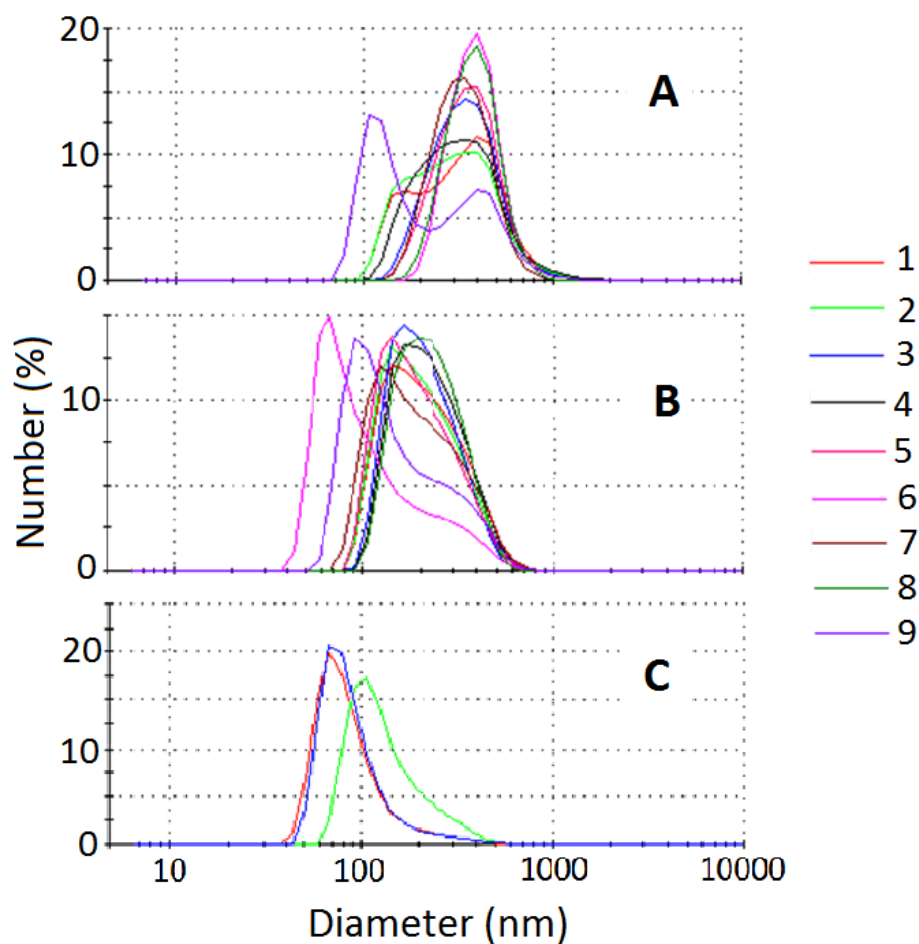


FIGURE 3.1: Number distribution of particle sizes at each stage of the preparation process: pre-acid treatment (**A**), post-acid treatment (**B**) and centrifuged (**C**). Legend shows measurements in chronological order.

### 3.1.2 Microscopy results: self-assembly

As mentioned before, the aim of this section was to produce high surface coverage, thin layers of diamond chemically bound to the Ti surface. Comparison of variations in the parameters in table 2.1 took the form of SEM image examination. Before discussing the results it is important to note that while each set of images is a fair comparison in itself, the parameters do not have stable optima to high order, *i.e.* changing one parameter may affect the optimum of another. Examples of this were challenging to detect, but they are pointed out where possible. All images are magnified by 1500 times unless otherwise stated (relative magnification only, not real image size).

Alteration of the first stage of the process, the use of MPA thiol, gave ambiguous results. The use of MPA occasionally gave positive results (a high coverage in a thin layer); however, as shown in figure 3.2 (**A/B**), the presence of MPA has reduced the coverage in some cases. That said, in the non-MPA case (figure 3.2**B**) there are more considerably sized areas of little deposition. Surface coverage estimates of both samples shown here are above 75%.

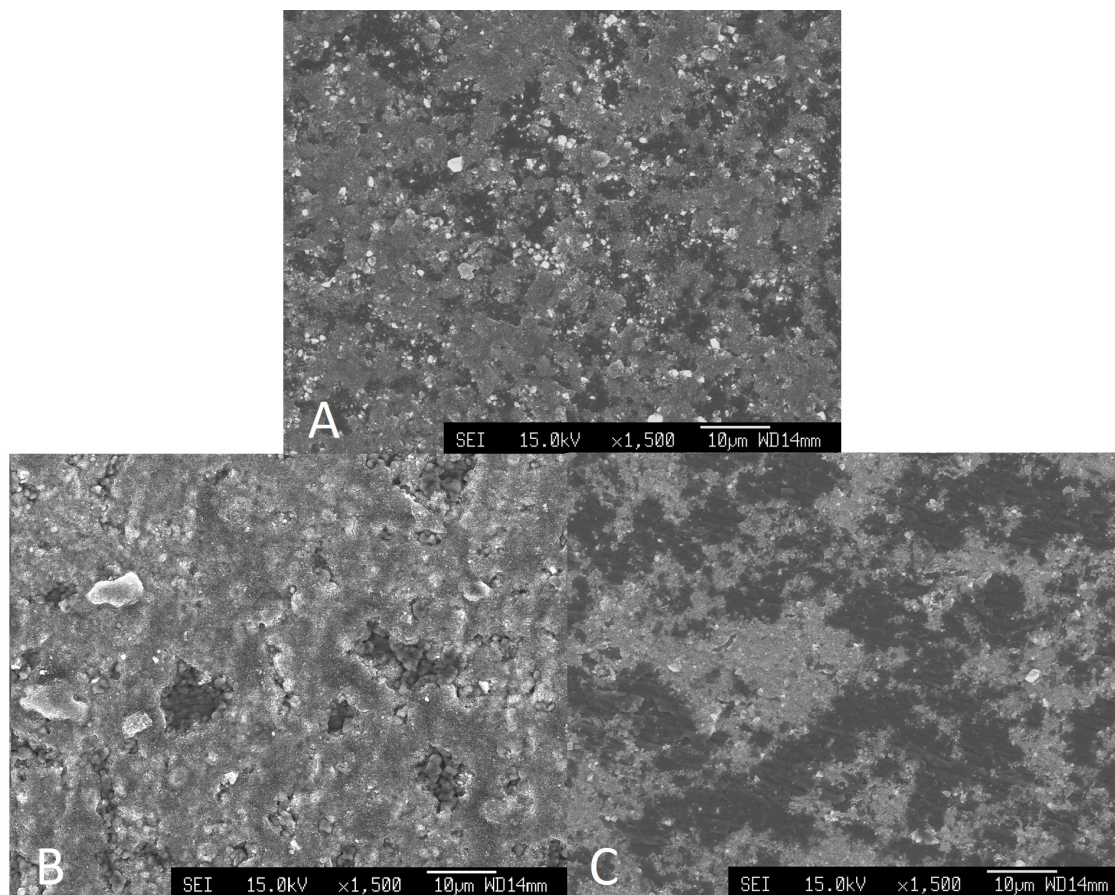


FIGURE 3.2: SEM (6330F) images comparing samples produced using/not using (A/B) MPA thiol, as well as samples produced using PEI solution v/m of 0.05% (A) and 0.1% (B).

The solution m/v of the PEI solution changed the coverage considerably. Figure 3.2 (A/C) shows this effect. The sample with the clearly higher surface coverage of around 75% is A, while C has only about 55%. This could be due to agglomeration of polymer on the surface at higher concentrations, leading to areas of higher and lower coverage of polymer, and in turn of diamond. Importantly, these samples utilised the MPA thiol, which may have affected the result. Other images (not shown) did show more positive results with higher polymer concentrations and no MPA. This means that the MPA may act as an enhancer to the polymer, requiring less polymer when used, potentially by spreading it more thinly over the already thin and extensive negatively charged layer. This is one example of an optimum affected by other parameters.

The results of changes in the molecular weight of the PEI in the polymer solution are shown in figure 3.3. There is little difference between the samples produced using the high and medium weight polymers, and all samples have 95%+ surface coverage. There is however, in the case of the low  $M_W$  polymer sample, a certain amount of aggregation of the diamond. These samples used diamond that had been sonicated for 6 hours, and then centrifuged, so would not be expected to contain aggregates of the sort seen in figure 3.3C. It is possible that the small size of the polymer molecules make them susceptible to solvating once again when the diamond suspension is drop cast

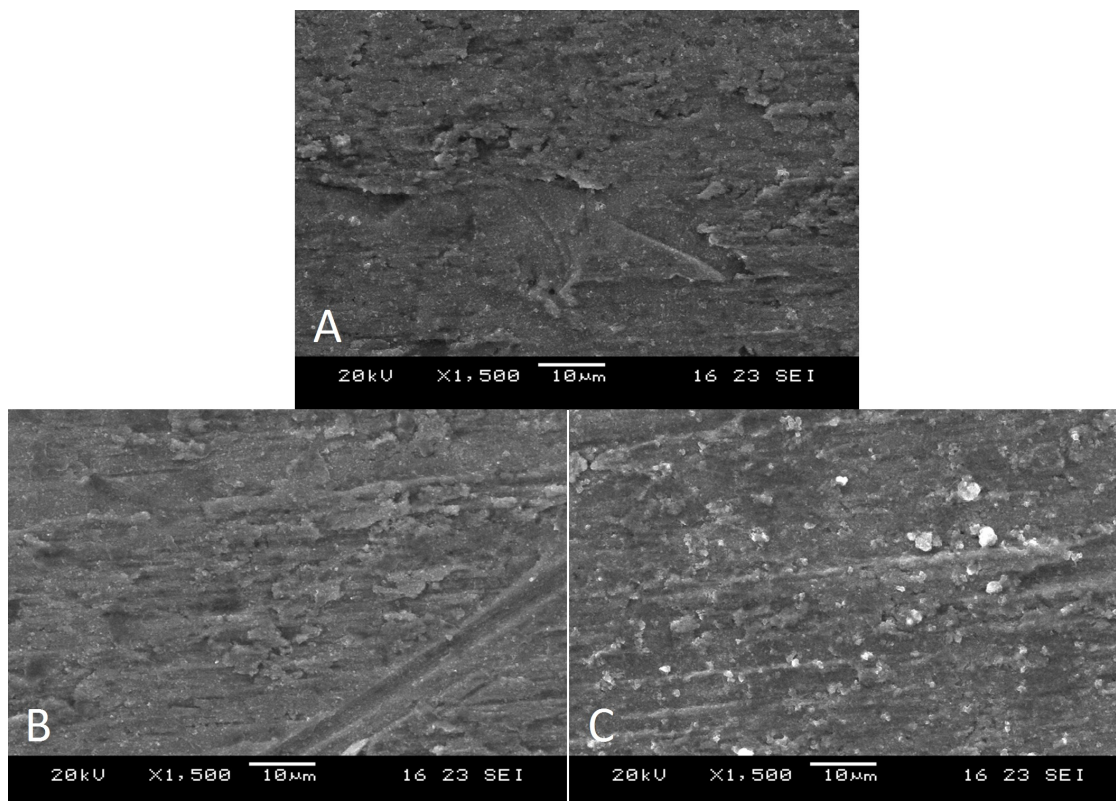


FIGURE 3.3: SEM (5600LV) images comparing samples produced with difference molecular weight ( $M_W$ ). **A** is  $800,000 \text{ g mol}^{-1}$ , **B** is  $60,000 \text{ g mol}^{-1}$  and **C** is  $1200 \text{ g mol}^{-1}$ .

on to the polymer coated surface. Potentially this could cause the low weight polymer to act as a flocculant to the particles during the deposition process, combining them to form large aggregates.

The images of samples produced by diamond suspensions sonicated for varying times gave results heavily affected by other parameters. The main affecting parameter being that the diamond suspensions were shaken prior to drop casting. This means that regardless of the size of the majority of particles, large particles were always deposited. Figure 3.4 shows this effect, where all samples display the presence of large agglomerates. Nevertheless, on close inspection it can be seen that there are differences in the composition of the smaller particles. Sample **A** shows abundant particles of size  $0.5 - 1 \mu\text{m}$ ; **B** shows fewer, and **C** fewer still. This, combined with the rational nature of the result, provides enough evidence to conclude that longer sonication times positively affect deposition particle size.

Similarly to the previous parameter, the diamond suspension  $m/v$  shows an optimum that is unstable when other parameters are changed. Figure 3.5 shows results obtained for this parameter, with clear differences between samples. Sample **A** shows a poor coverage of the surface, with some large aggregates but little spread of small particles. Sample **C** shows a high coverage, but with high levels of aggregates causing a multilayer of deposited diamond. These situations both being disadvantageous, sample **B** (0.2%) appears to be the optimum. This result was only found when,

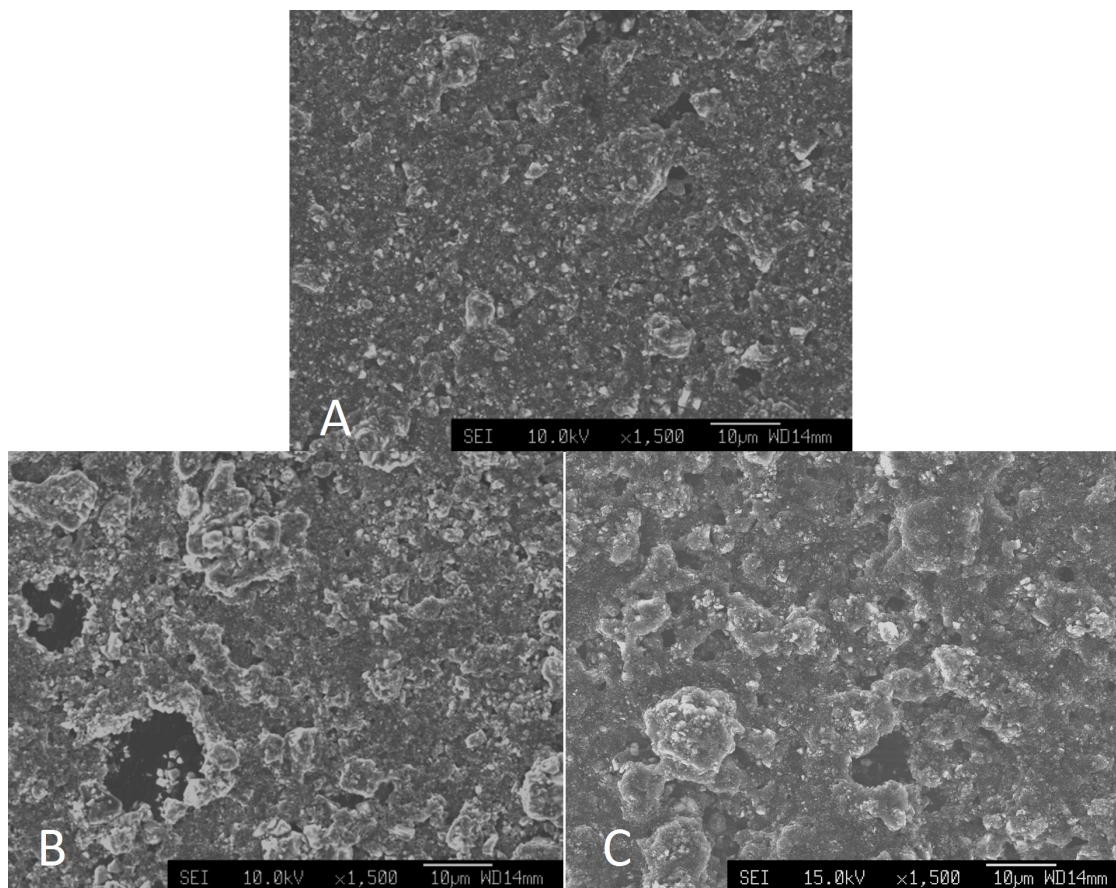


FIGURE 3.4: SEM (6330F) images comparing samples produced with varying sonication time periods. **A** is 1.5 hr, **B** is 3 hr and **C** is 6 hr.

as before, the sample was shaken. When using the top layer, or centrifuged samples (see below) the 0.5% suspension gave the best results.

As mentioned, the choice of shaken/top layer/centrifuged greatly affects the outcome of other results. Figure 3.6 shows the results obtained for this parameter. All samples here show high surface coverage ( $>95\%$ ), but their quality varies drastically. Clearly sample **A**, as shown before, shows a multilayer and therefore not an optimal diamond coverage. Taking the top layer of the suspension as in figure 3.6**B** gives a more even coverage, but still with large ( $0.5 - 1 \mu\text{m}$ ) particles. It would be reasonable to assume that a centrifuged sample would show the most even coverage of small diamond particles on the surface. In figure 3.6**C**, however, there are large visible aggregates, which show a charging effect (they are a lighter colour). These aggregates are therefore not making a conductive contact with the Ti substrate. The likely reason is that they are positioned on top of another layer of diamond on the surface. This is possibly because nano-diamond particles tend to be unstable in suspension due to their small size and high surface area [80], readily forming aggregates. With few larger particles for these aggregating particles to ripen, new ones nucleate. This would happen to particles that take the longest to deposit on the substrate because they are the smallest. When they finally sediment in aggregate form, they will sit on the top layer. Beneath

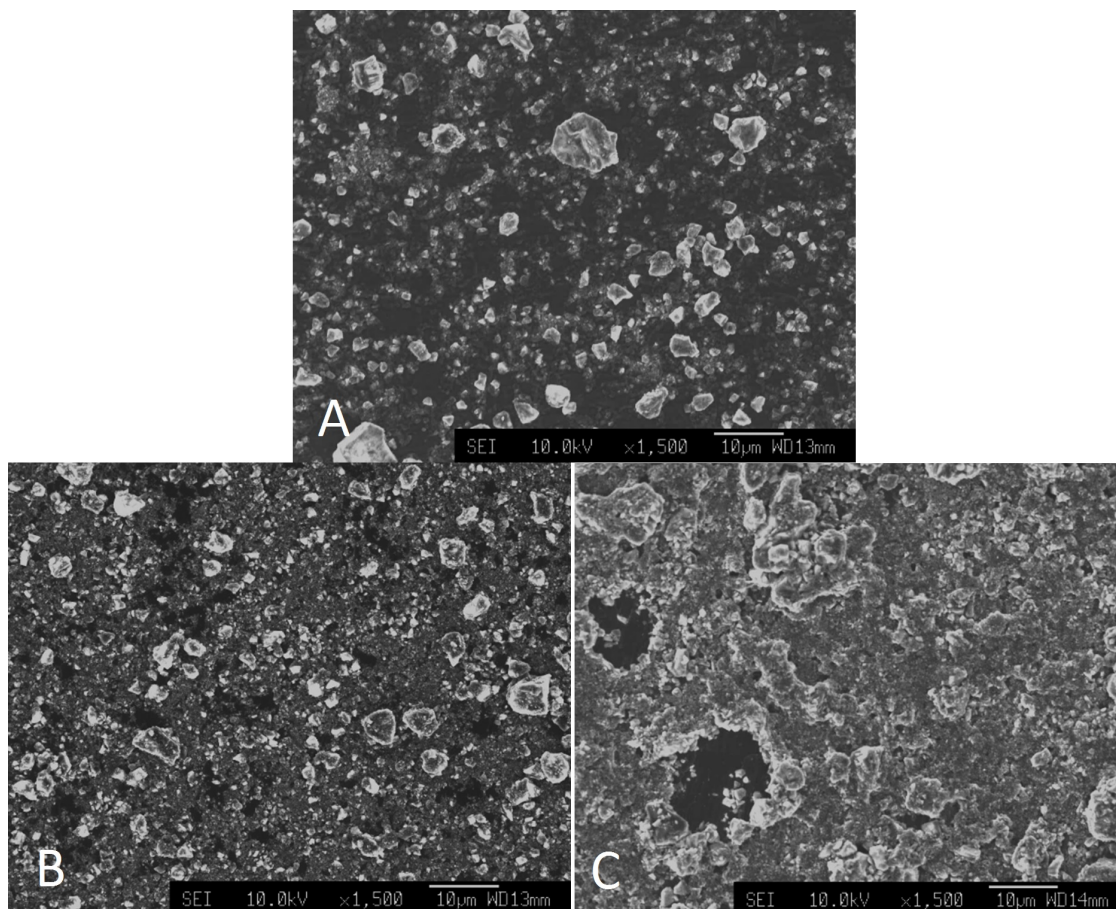


FIGURE 3.5: SEM (6330F) images comparing samples produced with a range of diamond suspension m/v. **A** is 0.1%, **B** is 0.2% and **C** is 0.5%.

these particles, however, there is (from more magnified images) a high coverage layer of small (<100 nm) particles. Larger particles like these (not well adhered to the substrate) are likely to be easily desorbed, so when the electrochemical measurements are taken, they are unlikely to affect results.

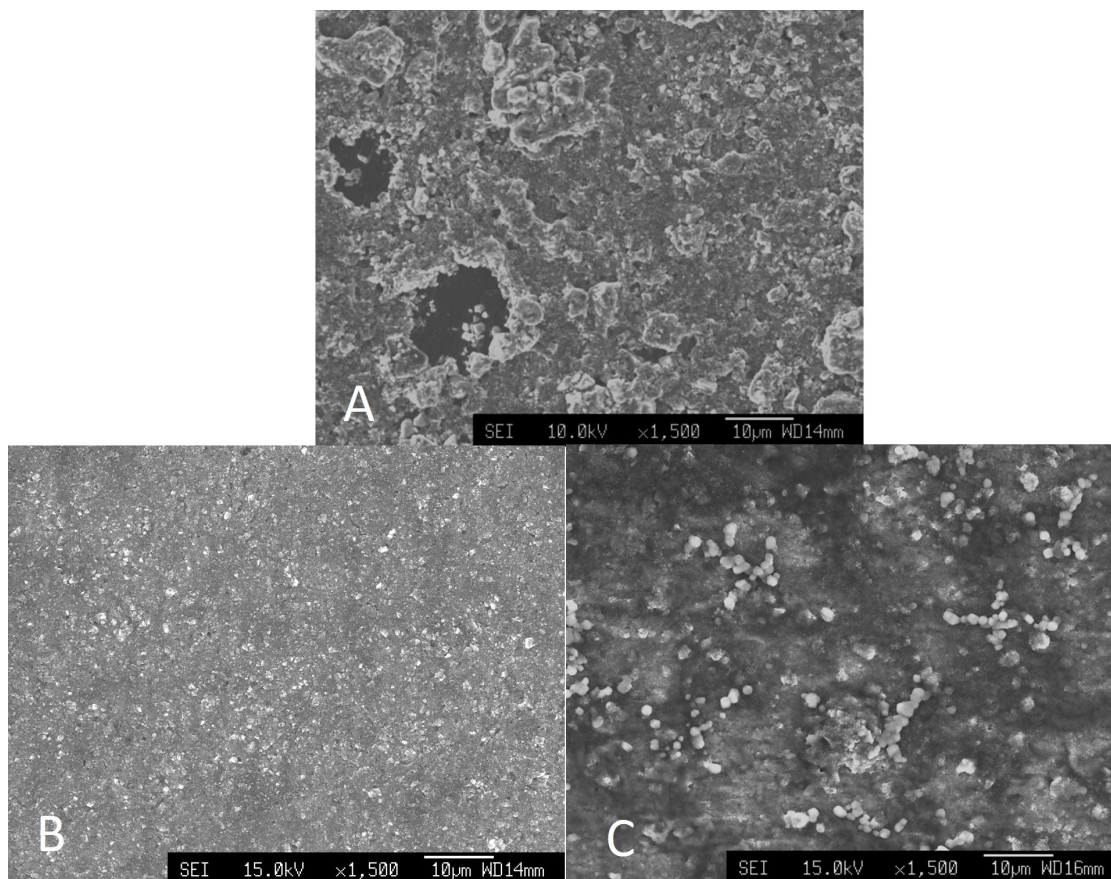


FIGURE 3.6: SEM (6330F) images comparing samples produced with diamond suspensions treated in different ways following sonication. **A** is a shaken sample, **B** is a top layer sample and **C** is a centrifuged sample.

Figure 3.7 shows images of samples annealed under various conditions. These samples had been sonicated in Milli-Q water for 30 second post-anneal. This removed excess diamond, as well as material that had not formed a strong chemical bond to the Ti. These images show clearly how increasing annealing time and temperature increases the coverage of well-adhered material. The solubility of carbon in titanium under CVD synthesis conditions is such that a thick TiC layer forms, resulting in weak adhesion [81]. This may not happen when using HPHT diamond particles as they were formed from  $sp^3$  diamond at the time of this process, but over long times there may have been more TiC formed than needed. At temperatures higher than 1000 °C, and for times longer than 90 s, the diamond was completely removed from the surface by the annealing process, confirming that strongest adhesion occurred when a thin but extensive TiC layer was formed at 950 °C for 90 s. For samples used in electrochemical measurements this post-annealing sonication method was not employed, in order to maximise the surface area of diamond; some of which may have been weakly, yet ohmically, bound to the substrate.

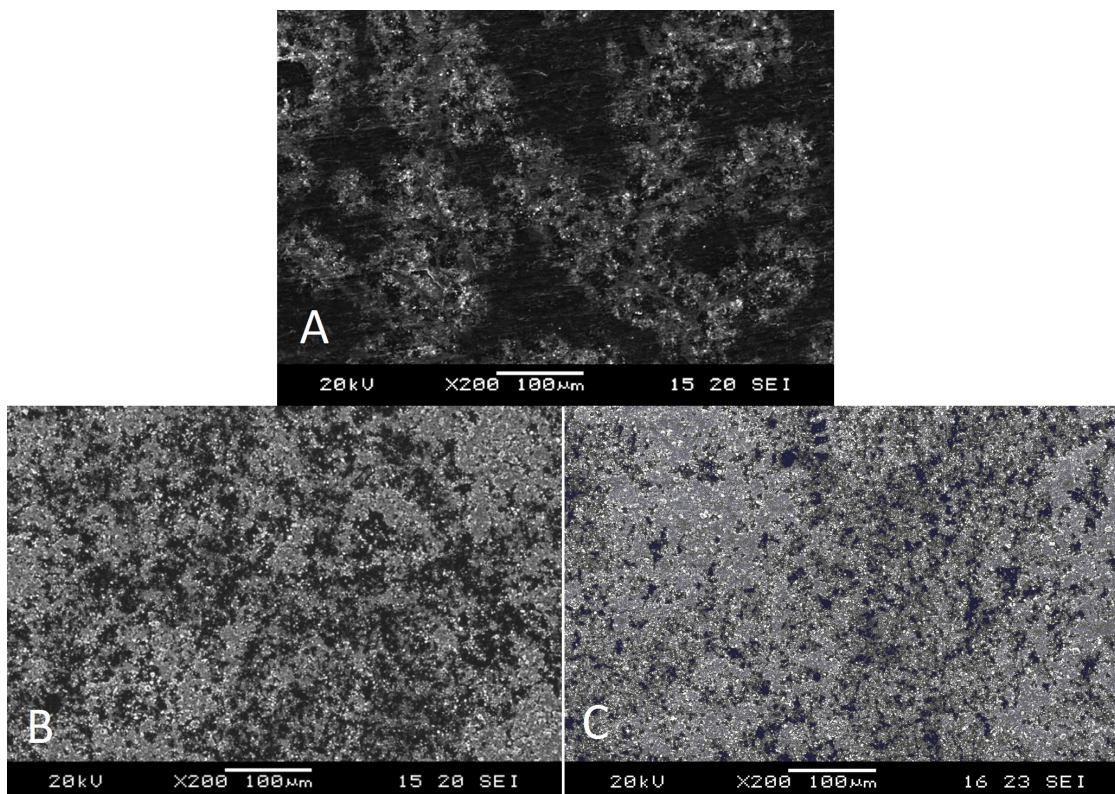


FIGURE 3.7: SEM (5600LV) images comparing samples annealed under different conditions. **A** had 30 s at 700 °C, **B** had 30 s at 900 °C and **C** had 90 s at 950 °C. Note the low magnification of these images, 200 times (relative).

The optimum values/options for each parameter are shown in table 3.1. Note that these are self-consistent, *i.e.* that each is the optimum when each of the others is also satisfied, unless otherwise stated.

| Process            | Parameter       | Optimum                  | Units                         |
|--------------------|-----------------|--------------------------|-------------------------------|
| MPA thiol          | Use             | See below                | –                             |
| PEI solution       | m/v             | 0.05 w. MPA, 0.1 w/o MPA | $\text{g dm}^{-3}/10$         |
| PEI solution       | Polymer $M_w$   | 60,000-800,000           | $\text{g mol}^{-1}$           |
| Diamond suspension | Sonication time | 6                        | hours                         |
| Diamond suspension | m/v             | 0.5                      | $\text{g dm}^{-3}/10$         |
| Diamond suspension | Treatment       | Centrifuged              | –                             |
| Annealing          | Temp. / time    | 950 / 90                 | $^{\circ}\text{C} / \text{s}$ |

TABLE 3.1: Sample fabrication optimum parameters. w. and w/o stand for ‘with’ and ‘without’ respectively. A range is given for the PEI  $M_w$  as no noticeable difference in performance was noticeable.

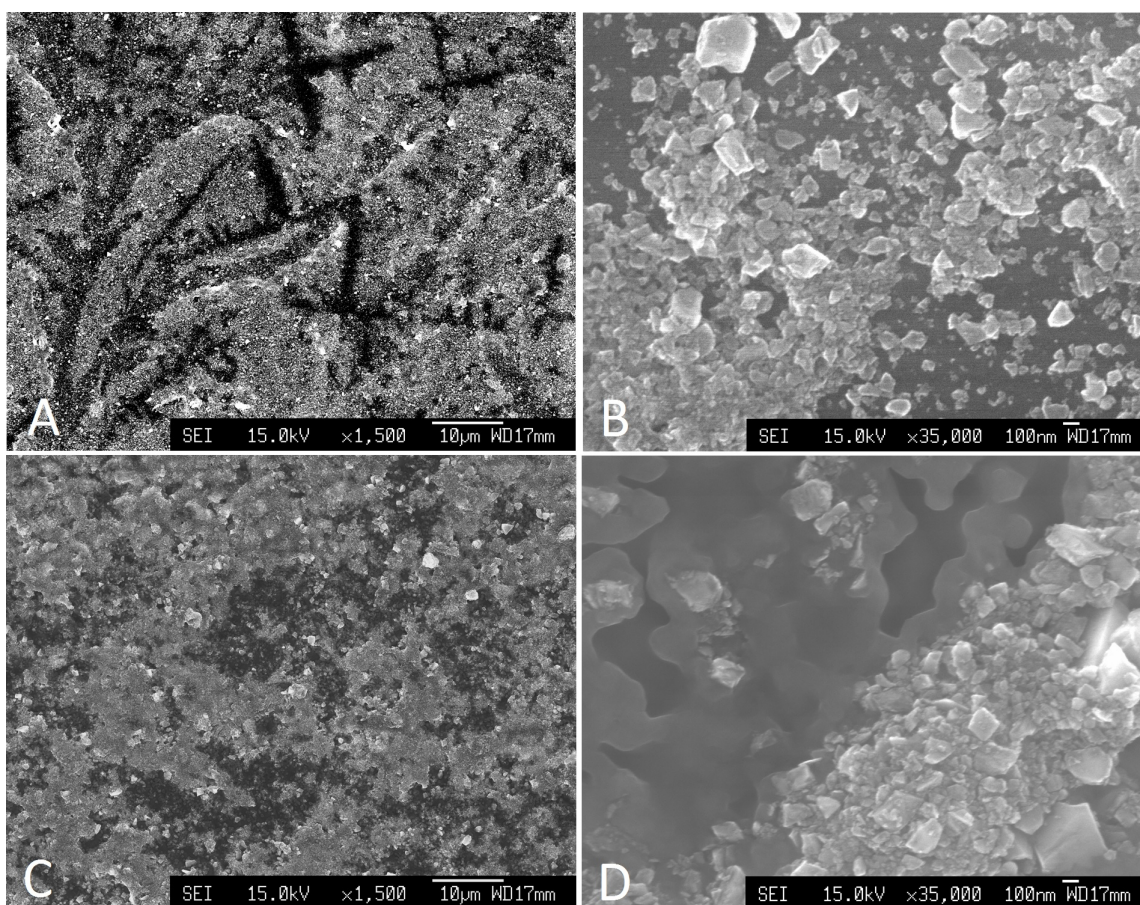


FIGURE 3.8: SEM (6330F) images comparing fabricated samples with different surface terminations. A is O terminated, B is O terminated (high magnification, 35,000 times), C is OLi terminated, and D is OLi terminated (high magnification, 35,000 times). Samples were fabricated using equal conditions.

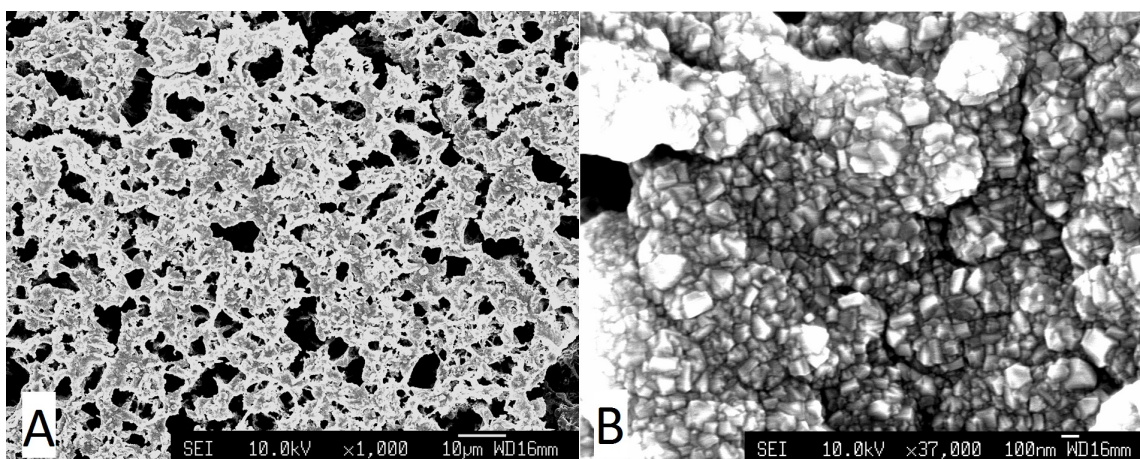


FIGURE 3.9: SEM (6330F) images showing Ti/CNT/BDD samples with H surface termination. A and B show images of similar magnification to figure 3.8 left and right respectively.

### 3.1.3 Microscopy results: surface termination

SEM was used to compare samples of differing surface terminations. Figure 3.8 shows fabricated samples after ozone treatment, and for **C** and **D** after subsequent lithiation. From the low magnification images, **A** and **C**, it is clear that the lithiation process works to smear the surface somewhat, in that **C** has less well defined particles/areas that show the metallic substrate. This is confirmed by comparing **B** and **D**, where the latter shows a lighter tone surrounding the diamond particles. This is comparable to a wetting scenario, where the surface tension of a liquid (in this case lithium before solidification) causes it to collect in and around crevices. An important factor in these images is that if the surface termination is truly different, then in the SEM they will act differently. This is due to the surface dipole shifting the work function of the material, and can often manifest itself in altering the saturation of SEM images.

Figures 3.8 **B** and **D** show the effect of image alteration, which is explained as follows. As shown in the figure, the accelerating voltage for incoming electrons in the SEM is 15 kV, giving the electrons 15 keV of energy. This means that regardless of the surface dipole, they will enter the material surface and ionise multiple atoms. Secondary electrons produced by chain-ionisation of atoms have a still high but much smaller (and broader) range of energies. For these electrons, dipoles do alter the ejection process in a small but detectable way. Referring to section 1.4.2, an electron of relatively low energy is more likely to be emitted through a surface of low work function (and NEA) than one of high work function (without NEA) [82]. This means that OLi terminated surfaces should more efficiently emit secondary electrons than O terminated surfaces. Returning to figure 3.8, **D** shows diamond particles in high resolution and not much charging (light tones). Whereas, in **C** there is a high contrast between light and darker diamond particles, and a lower resolution. This is evidence for the enhanced secondary electron emission in **D** compared to **C**, caused by the reduced work function and the NEA in the OLi terminated sample [71].

Figure 3.9 shows as-grown porous samples with hydrogen termination. As with the previous figure, the highly magnified image (**B**) shows high resolution. In addition, however, it does show charging effects. A possible cause of this is that CVD diamond grew to a thicker layer, with more defects  $\text{cm}^{-2}$ , in some areas, rendering it less conductive and prone to charging. These areas would likely be the tips of CNT clusters, where the porous structure protrudes further from the substrate, and deposition occurs more readily. It is unclear from these images what the exact structure of the CNT scaffold is, as these images show no consistent teepee structure. However, it is clear that the structure is highly porous, giving it a large surface area. In addition, the surface coverage is consistently high, and darker areas on figure 3.9**A** could potentially be covered by CNTs as opposed to exposing the substrate.

The use of these three differing terminations in comparative measurements may be flawed quantitatively due to their vastly different characteristics. However, in *qualitative* comparison of

electrochemical and photoelectrochemical measurements, their use is valuable. Henceforth then, measurements and discussions involving these samples will be concerned with the qualitative effect of their termination. This makes the reasonable assumption that the diamond is of similar chemical and electronic character, as the doping concentrations and crystallite sizes are of the same order. Some qualitative performance comparison can be made between O and OLi terminated samples, as they have both been produced using the optimum conditions detailed in table 3.1, with the caveat that thiol was not used for samples in the results shown following.

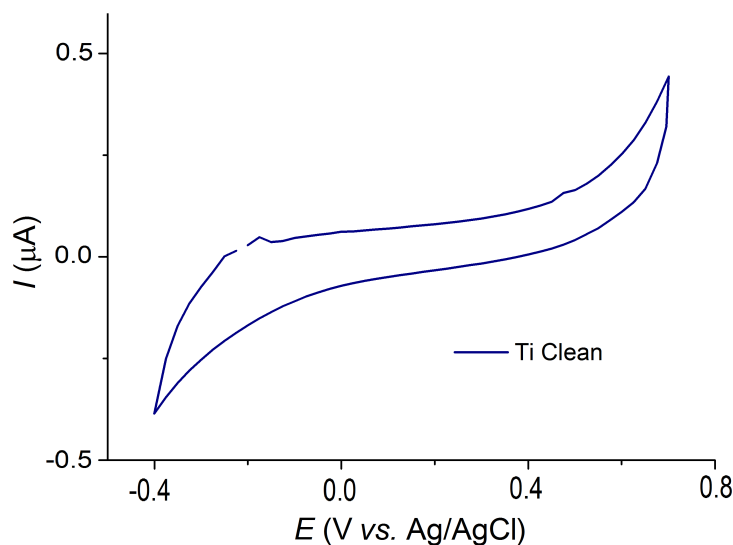


FIGURE 3.10: Cyclic voltammogram of Ti substrate in KCl. Scan rate =  $50 \text{ mv s}^{-1}$ .

## 3.2 Electro/Photoelectrochemistry results

### 3.2.1 Cyclic voltammetry and Xe lamp chronoamperometry in KCl

Cyclic voltammograms (CVs) were used to identify regions of applied potential in which the electrodes were stable and where no electrochemical reactions take place in the dark. The extremes of these plots are oxidation (positive current) and reduction (negative current) reactions. KCl is used as the primary electrolyte here as it does not undergo reduction or oxidation at the potentials probed here. All potentials (in units of V) following are given against the Ag/AgCl reference potential.

As there was substrate exposed on most of the electrodes examined, it was necessary to take measurements using clean Ti in order to show how the substrate contributes to the results. This CV is shown in figure 3.10, in which there is a clear, horizontal window in which no processes are occurring. The extremes in figure 3.10 correspond to the oxidation of water ( $E > 0.6 \text{ V}$ ) and the reduction of protons ( $E < -0.3 \text{ V}$ ).

Similarly to the substrate CV, those using fabricated electrodes show oxidation and reduction peaks at extreme potentials. For measurements taken in KCl, shown in figure 3.11, the upper limit occurs at  $0.6 \text{ V}$ . With these electrodes the reduction onset potential is around  $-0.1 \text{ V}$ , which indicates that the electrodes are in some way enhancing the reduction process compared to the pure Ti substrate. Whether this is due to their enlarged effective surface area (roughness) or their electronic properties is unclear. A point to note on all CVs comparing the Ti/CNT/BDD (0.1H and 0.2H) and Ti/TiC/BDD (O and OLi) electrodes is that the enormous surface area of the former causes a much greater capacitance than the latter. In this case, capacitance is the storage of charge at the

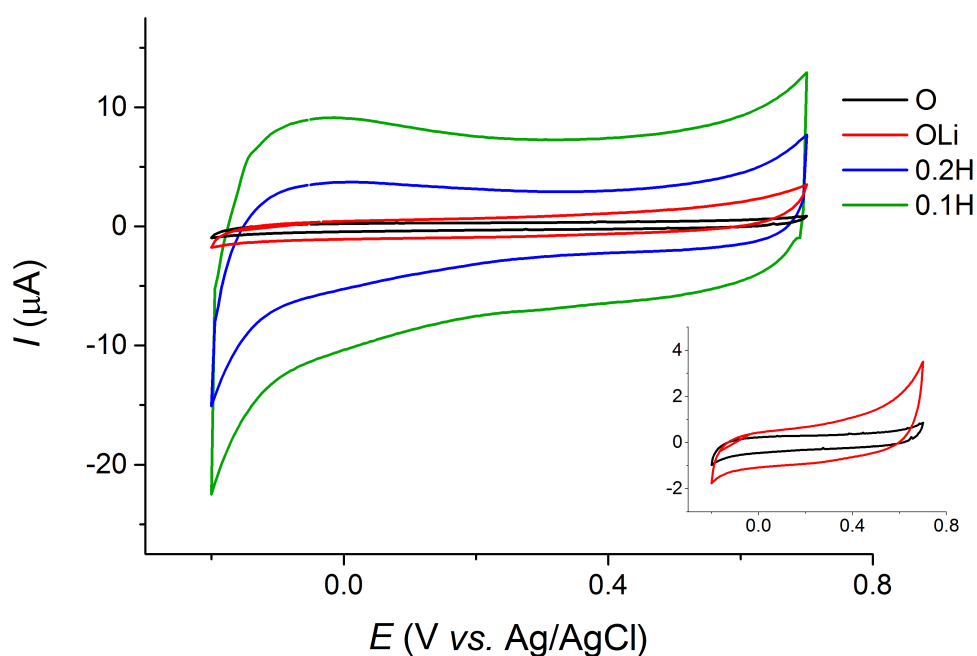


FIGURE 3.11: Cyclic voltammograms of each studied sample in 0.1 M KCl solution. The inset shows the O and OLi samples on an expanded  $I$  axis, units are the same as the main plot. Scan rate =  $50 \text{ mv s}^{-1}$ .

electrode surface, and these porous BDD electrodes are noted for their high capacitance values [69]. This has the effect of vertically broadening the CV plots, showing positive currents on increase, and negative currents on decrease of potential. This is the reason for the required inset to show the shape of the O and OLi CVs.

Having established a potential window over which photoelectrochemical measurements could be taken (-0.1 to 0.6 V), chronoamperometry showed how photocurrent evolved over time. A selection of potentials within the determined window gave plots as shown in figure 3.12.

The first important note here is that there are clearly two processes contributing to the photocurrent plots in figure 3.12. Firstly, immediately following illumination there is as expected a prominent and almost vertical change in the current, referred to hereafter as the ‘spike’. The second process, a gradual change in the photocurrent, is hereafter referred to as the ‘decay’. Qualitatively, the 0.2H and 0.1H (Ti/CNT/BDD structured) samples show vastly different characteristics to the OLi and O (Ti/TiC/BDD structured) samples. For example, their plots (**A** and **B**) show a positive spike in photocurrent following illumination, before decaying to negative values at all but positive potentials. Whereas in the OLi and O samples (**C** and **D**) the spike is negative, and the decay here appears to be termination dependent. The decay in the OLi terminated sample (clearly visible in the -0.1 V plot) is similar to that of the 0.1H and 0.2H samples, in that it is progressing negatively. This could suggest that the NEA surface termination plays a role in the longer term photocurrent properties.

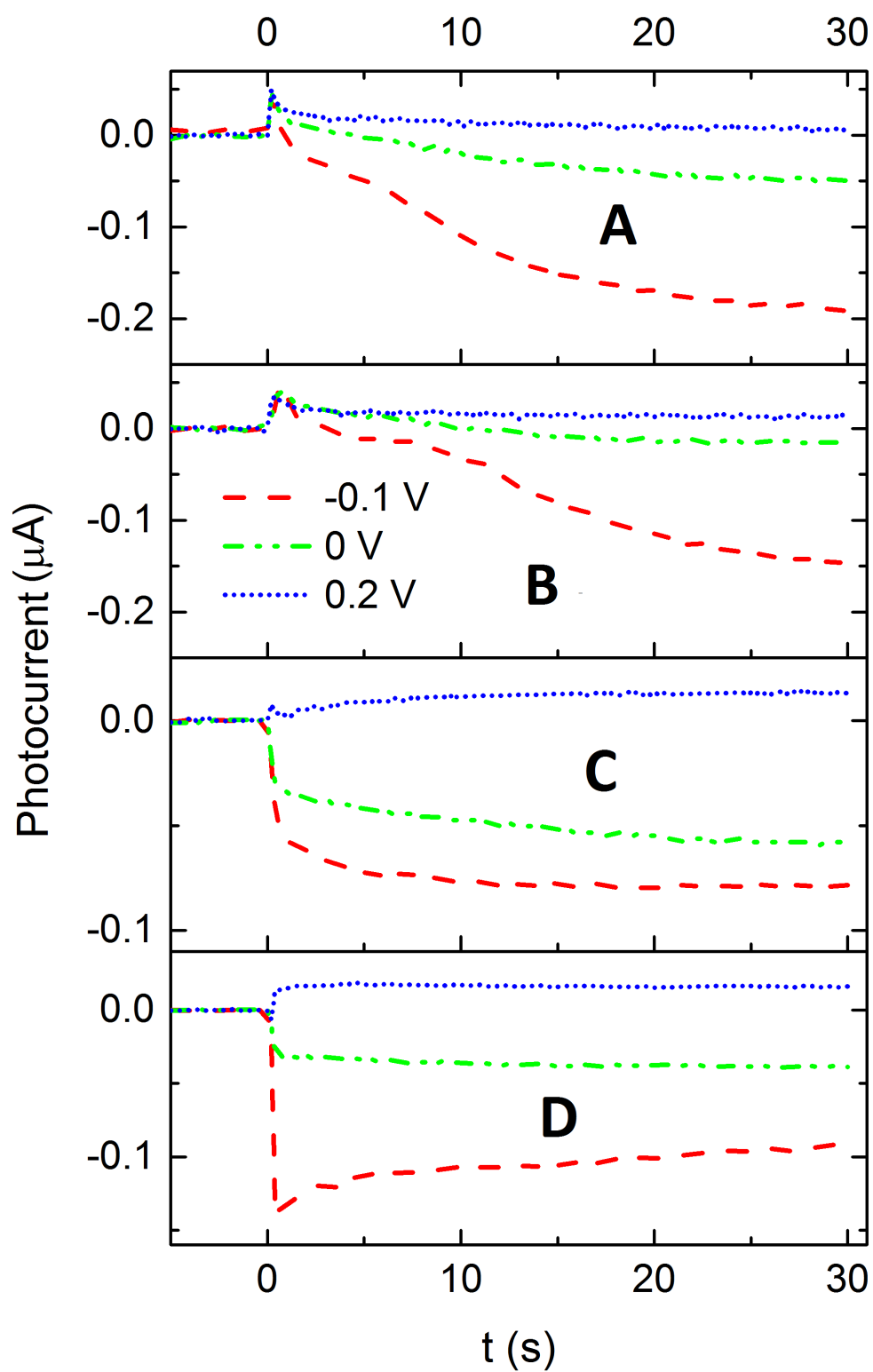


FIGURE 3.12: Compiled chronoamperometry in 0.1 M KCl with xenon arc lamp illumination commencing at 0 s. **A** is 0.2H, **B** is 0.1H, **C** is OLi and **D** is O. The red dashed line is at -0.1 V, the green dashed and dotted line is at 0 V, and the blue dotted line is at 0.2 V, each *vs.* Ag/AgCl.

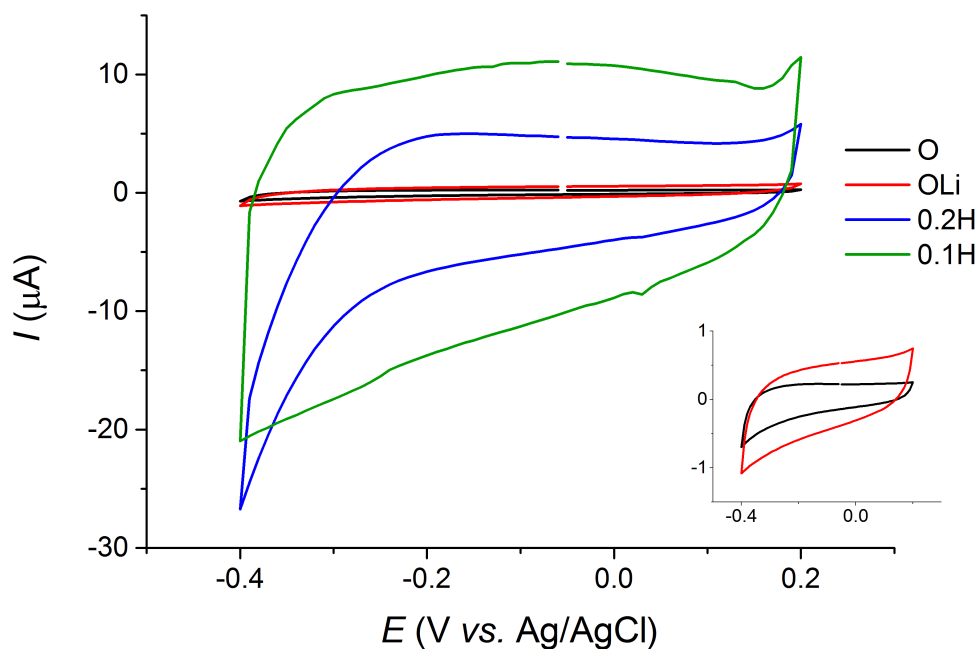


FIGURE 3.13: Cyclic voltammograms of each studied sample in 0.1 M  $\text{Na}_2\text{SO}_3$  solution. The inset shows the O and OLi samples on an expanded  $I$  axis, units are the same as the main plot. Scan rate =  $50 \text{ mV s}^{-1}$

Equally, the similarities in the O and OLi samples compared to the 0.1H and 0.2H samples could show that the bulk properties of the diamond samples determine the short term photo-effects.

The higher level of doping in the 0.2H sample than in the 0.1H appears to manifest itself in figure 3.12. The negative decay at -0.1 V in 0.2H is greater in magnitude than that of the 0.1H sample, and the positive spike at 0.2 V in 0.2H is also greater in magnitude. This is confirmation that increased levels of doping increases conductivity through increasing carrier concentration.

Whatever the cause of the dual-process photocurrent, it is clear that it exists. Accelerating either the positive or negative photocurrents could give an insight into the processes. For this reason it was necessary to probe the system using an electrolyte that scavenged charge carriers. Due to the unexpected positive spikes,  $\text{Na}_2\text{SO}_3$  was used as a hole scavenger, attempting to enhance the response.

### 3.2.2 Cyclic voltammetry and Xe lamp chronoamperometry in $\text{Na}_2\text{SO}_3$

As a hole scavenger  $\text{Na}_2\text{SO}_3$  is able to speed up the kinetics of positive photocurrent as the sulphite ion is readily oxidised to sulphate [83]. As shown in figure 3.13, it also allowed the probing of more negative potentials: in general the onset of cathodic current was -0.3 V. As the electrolyte solutions were not buffered, this could be due to Nernstian pH effects, which change the reduction potential

by - 59 mV per unit of pH [84]. As  $\text{Na}_2\text{SO}_3$  is a mild acid, these measurements qualitatively agree with this concept.

At small positive potentials of 0.15 to 0.20 V,  $\text{Na}_2\text{SO}_3$  causes an oxidation current, and as this was not present in KCl, this suggests an electrolyte reaction is occurring. This represents the non-reversed oxidation of  $\text{Na}_2\text{SO}_3$ , and sets an upper limit for probing positive photocurrents, which occur more strongly at positive potentials.

In figure 3.13 the large capacitive current is present, as was also present in the KCl CVs. However, here the 0.1H and 0.2H samples appear to behave differently, in that there is a pronounced reduction current onset at -0.3 V in the 0.2H sample that is not present in the 0.1H sample. The larger capacitive current in the 0.1H sample is potentially masking this reduction process, preventing it being detected whilst still occurring. The larger apparent capacitance at negative potentials could be in fact associated with a reduction of protons and re-oxidation of hydrogen radicals that does not manifest itself as peaks, but still contributes to the current. The reason for this effect being present in one sample but not others is unclear.

Using the potential window set by CV measurements (-0.3 to 0.15 V), chronoamperometry measurements with illumination are shown by figure 3.14. The hole scavenger nature of the electrolyte is clear in these plots. For example the 0.1H sample does not decay to negative photocurrents even at relatively large negative potentials, the decay of both the O and the OLi samples completely eliminates the negative photocurrent, and the positive spike in 0.1H and 0.2H is more prominent.

The 0.1H and 0.2H plots in KCl were closely related but here they are vastly different. The decay in the 0.2H sample is similar to that in KCl, but in the 0.1H sample in 3.14 the negative potentials do not appear to alter the decay compared to the 0 V plot.

There are similarities between figure 3.14 and its KCl counterpart. For example, at the highest potential the O and OLi plots (here 0 V) show a stronger positive photocurrent in the former, which is also of higher magnitude here than in KCl. One surprising feature is that the negative spike in the O and OLi samples in  $\text{Na}_2\text{SO}_3$  is larger than in KCl. In addition, the negative photocurrent caused by the decay in 0.2H is also much larger in  $\text{Na}_2\text{SO}_3$ . This is possibly due to the physical set-up of the apparatus, causing a greater intensity illumination in the measurements shown in figure 3.14.

The increase in spike magnitude in 0.1H, O and OLi as well as the vast change in decay properties in these samples on changing the electrolyte to  $\text{Na}_2\text{SO}_3$  confirm the distinct nature of the two processes. Both of these figures (3.12 and 3.14) show that the two processes involved in producing photocurrent occur on different timescales. Two distinct processes could be a result of two different areas of the broad spectrum (see the appendix) interacting with the diamond surface in different ways. This could signify that one process occurs due to surface states and one due to bulk mobilisation of

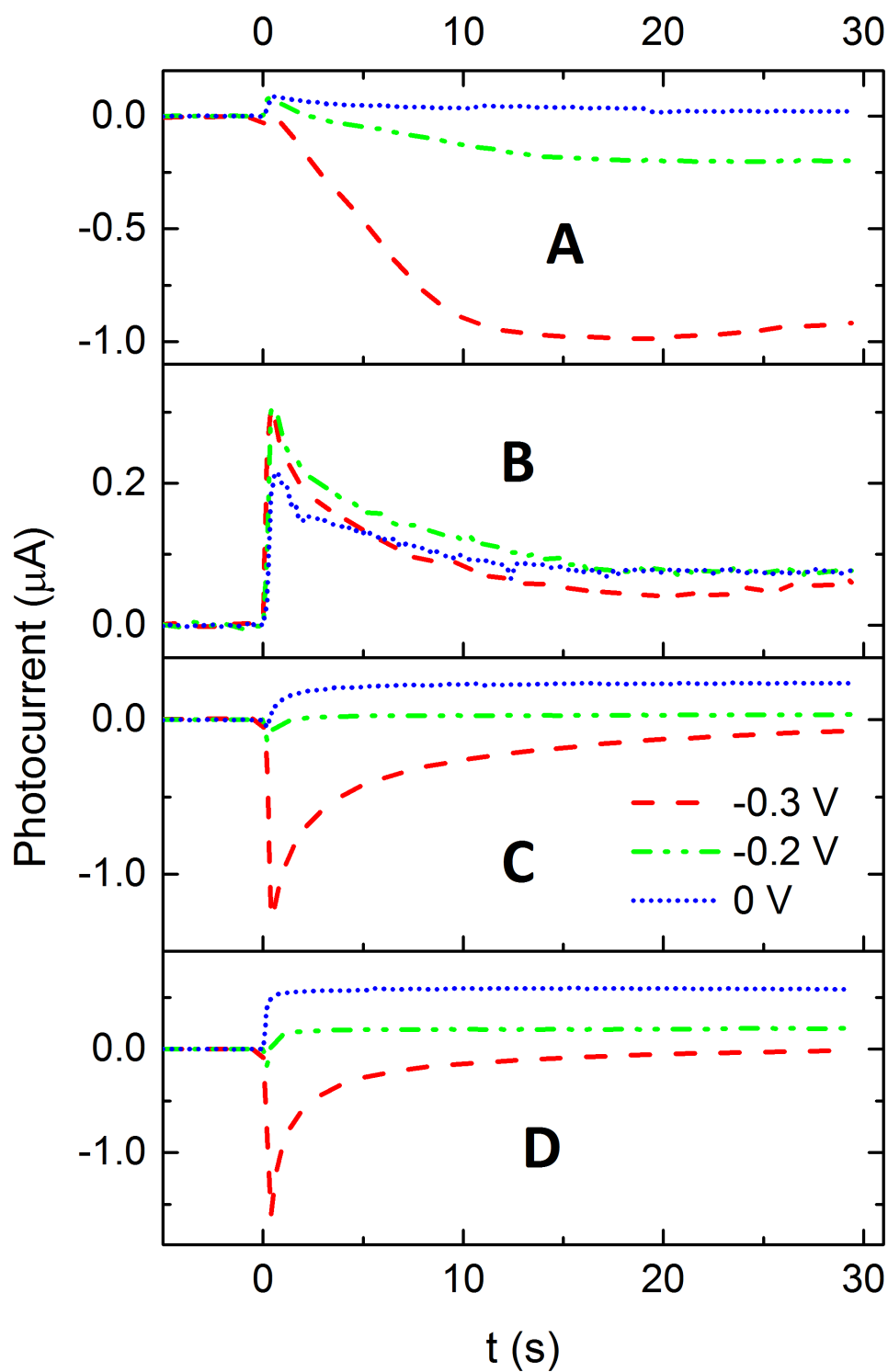


FIGURE 3.14: Compiled Chronoamperometry in  $0.1 \text{ M Na}_2\text{SO}_3$  with xenon arc lamp illumination commencing at  $0 \text{ s}$ . **A** is  $0.2\text{H}$ , **B** is  $0.1\text{H}$ , **C** is  $\text{OLi}$  and **D** is  $\text{O}$ . The red dashed line is at  $-0.3 \text{ V}$ , the green dashed and dotted line is at  $-0.2 \text{ V}$ , and the blue dotted line is at  $0 \text{ V}$ , each *vs.*  $\text{Ag}/\text{AgCl}$ .

charge carriers. However, the xenon arc lamp outputs sub band-gap radiation for diamond, meaning that only surface states can be active under its illumination.

Whether the HER is occurring is unclear. One possibility is that the sign of the spike (positive or negative) could be based on the presence of oxygen or hydrogen atoms. Regardless of the electron affinities of the materials, each sample containing surface oxygen has mostly negative spikes, and each containing hydrogen has mainly positive spikes. This in fact agrees with early work concluding that oxygen termination is advantageous for reduction photoelectrochemistry due to a flat-band potential increase [64]. It also suggests that the OLi surface is in fact electronically closer to that of the O sample than to the 0.1H and 0.2H samples. There is a possibility that the lithiation process has not been fully successful in providing the extensive OLi termination hoped for.

Ideally, measurements of the photocurrent should be measured consistently, and at a range of potentials, *i.e.* photocurrent-voltage spectra. However, with the time-scale of the photocurrents here, it would give few valuable results. For this reason, and because the xenon arc lamp produces sub band-gap radiation only, the argon-mercury discharge tube was employed.

### 3.2.3 Cyclic voltammetry in $\text{EuCl}_3$ and Ar-Hg lamp chronoamperometry

As mentioned in section 2.3, the 0.1H and 0.2H samples suffered from poor connection in the electrodes caused by prolonged use. For this reason, measurements from here onward show results from only the O and OLi samples. These samples were also probed in a third electrolyte in order to provide knowledge on negative photocurrents, an electron scavenger:  $\text{EuCl}_3$ . In order to gauge the stable electrode potential window, CVs were plotted and are shown in figure 3.15. These CVs show that the potential window for  $\text{EuCl}_3$  photocurrent measurements is between roughly -0.2 and 0.5 V.

Chronoamperometry measurements were recorded and plotted as shown in figure 3.16, using the Ar-Hg discharge tube as the light source. As mentioned, this lamp could not be proven to produce radiation corresponding to its spectral peak at 185 nm [85], being beyond the range of the UV-Vis spectrometer. The smell of ozone did suggest that this wavelength was being emitted, but its propagation distance was not measurable.

Whilst not showing any quantitative results due to the variation in applied bias across its three plots, figure 3.16 does show a surprising change in the evolution of photocurrent over time. Either the decay process magnitude has been almost entirely eliminated or the decay has been accelerated, so happens alongside or just after the spike. The reason for this is unclear, but if there is band-gap illumination occurring (and if there is it is minute, judging by the magnitude of the response) then it is completely masking any other processes caused by the sub band-gap light as discussed in the previous sections. There is however, still some decay over time, but not enough to remove the

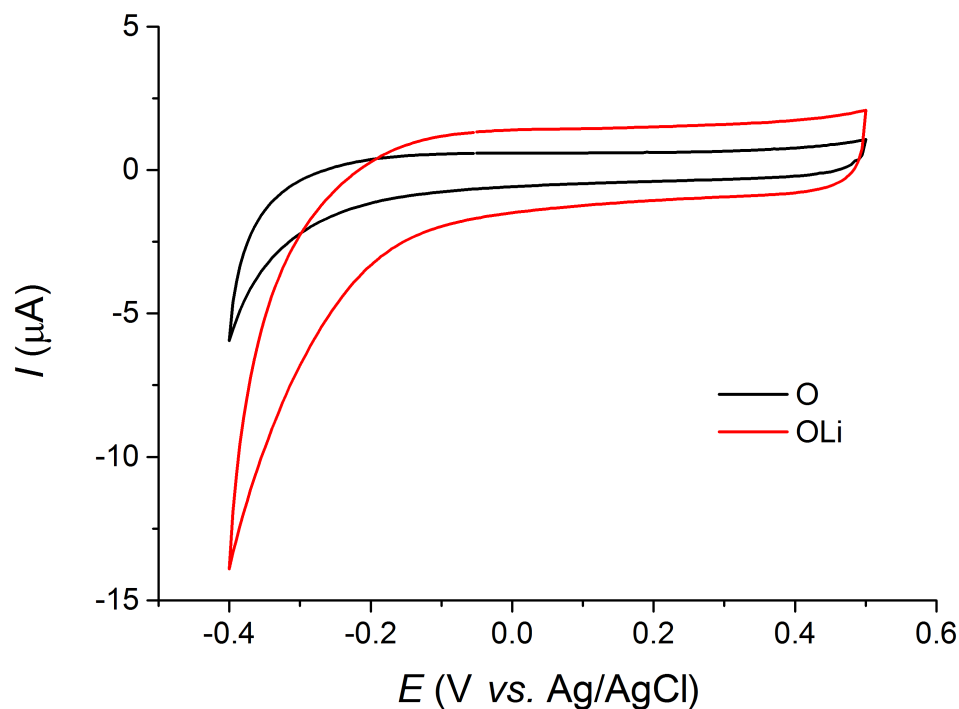


FIGURE 3.15: Cyclic voltammograms of O and OLi samples in 0.1 M  $\text{EuCl}_3$  solution. Scan rate =  $50 \text{ mV s}^{-1}$ .

possibility of using lock-in amplified photocurrent-voltage spectrum measurements. Thus figure 3.16 serves to justify the use of the following technique and its results.

### 3.2.4 Photocurrent-voltage spectra

The results shown in figure 3.16 show rapid evolution of the photocurrent to its maximum. Therefore, it was justifiable to approximate the photocurrent as entirely real. This approximation required that equation 2.1 was used to rotate the imaginary part of the photocurrent by however much renders its plot horizontal. This value of  $\theta$  was equal for each case to  $3.07 \pm 0.05 \text{ rad}$ . In making this correction, the real part of the photocurrent is also rotated in the imaginary plane, and the resulting two plots are shown for each electrolyte-sample combination in figure 3.17.

In each plot in figure 3.17 the dependence of the photocurrent on  $E$  is roughly linear. This can be attributed to the degenerate nature of the diamond particles. With such a small value of  $W$ , the physical property changed by the bias is the Helmholtz layer as opposed to the band-bending within the material. This confirms that the Gartner equation (1.7) does not satisfactorily describe these diamond electrodes, and their potential-induced behaviour is more suitably described by metal electrochemistry. The linearity in both positive and negative photocurrent shows that photoelectrochemical processes on these electrodes can be oxidation reactions as well as reduction

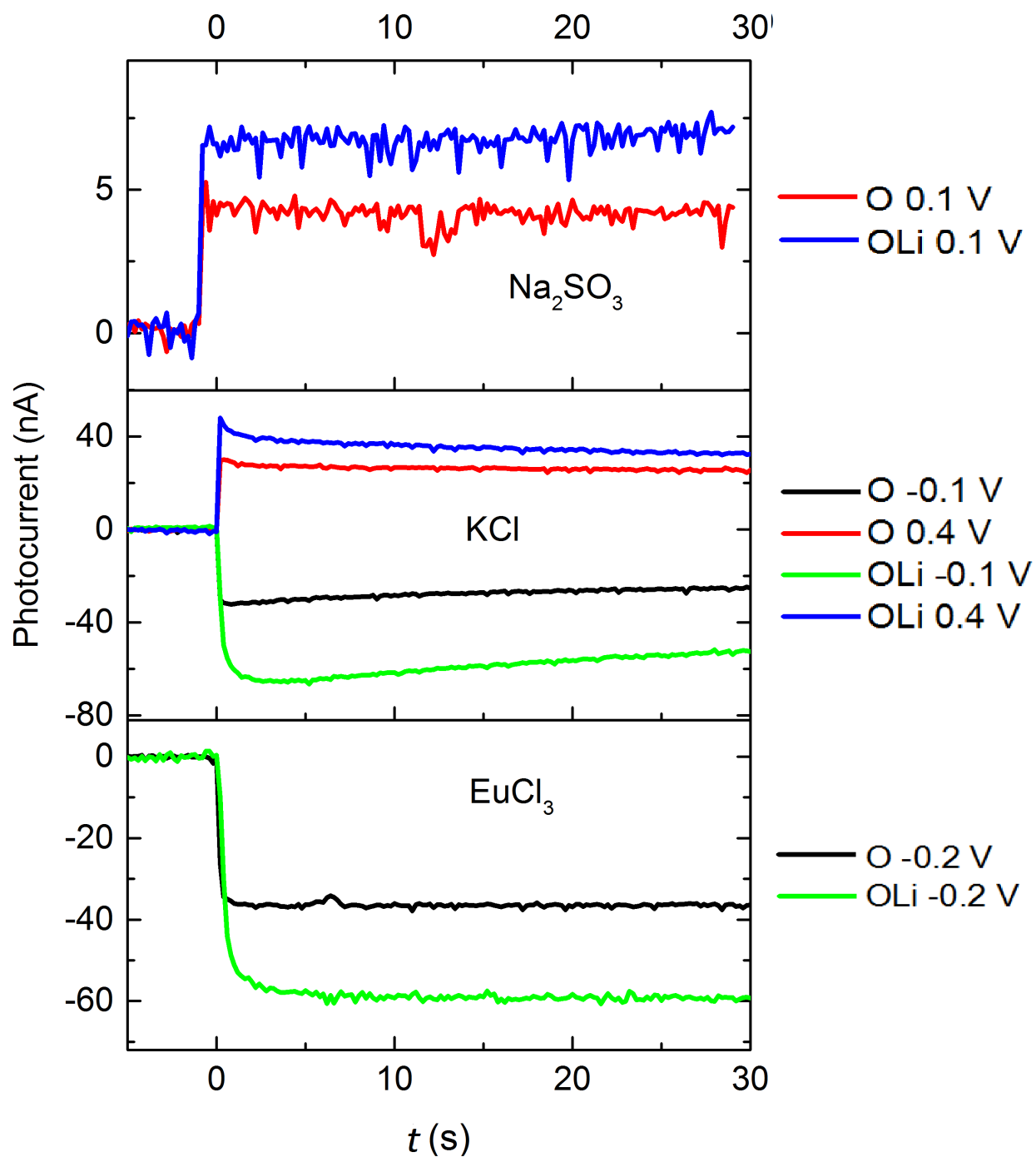


FIGURE 3.16: Compiled Chronoamperometry in each electrolyte with Ar-Hg discharge lamp illumination commencing at 0 s. Note that all potentials are different for the different electrolytes, and are measured against the Ag/AgCl reference.

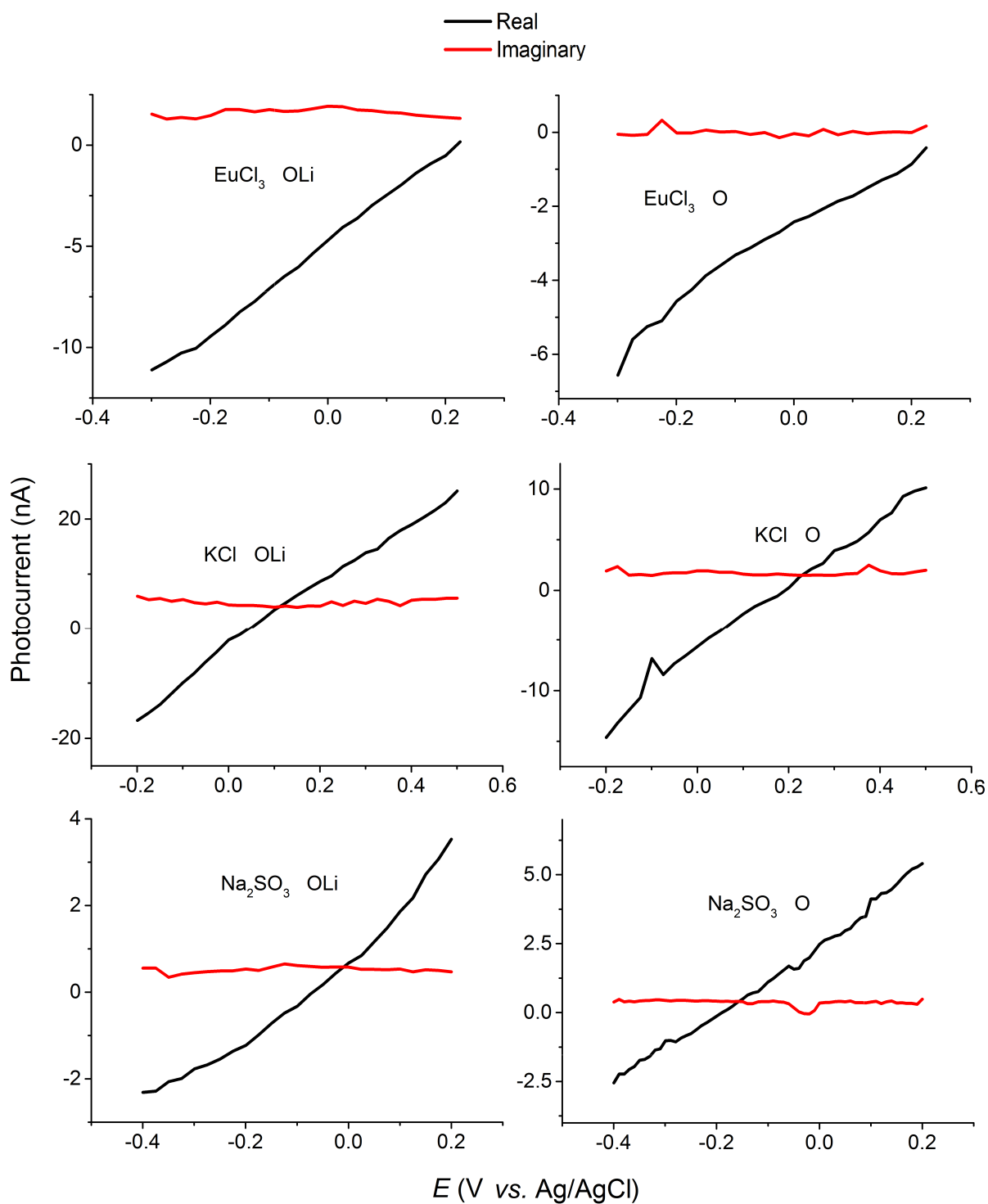


FIGURE 3.17: Photocurrent-voltage spectra for O and OLi samples in each electrolyte. Measurements taken with lock-in amplifier.

reactions. This depends on the potential, the electrolyte and in an apparently small way the surface termination.

The plots in figure 3.17 provide two comparisons between the two electrode terminations. These come firstly from the gradient of the plots, and secondly from the potential at which the photocurrent changes sign, analogous to  $E_{FB}$ . Both of these quantities are electrolyte dependent, and similarly to the reduction potential of hydrogen, they may also be pH dependent. The gradient is also dependent on the actual sample surface area as well as the light modulation frequency, to which the photocurrent is very sensitive. However, considering the sample production was the same and their measurement light frequency was definitely within the range 1.2 to 1.4 Hz, comparisons can be made.

With the exception of  $\text{Na}_2\text{SO}_3$ , in each electrolyte the OLi terminated sample shows a stronger photocurrent gradient than the O sample. Reasons why this is not the case for  $\text{Na}_2\text{SO}_3$  are unapparent; this is not due to light modulation frequency. The frequency in the O measurement was marginally higher than in the OLi. However, this measurement does agree with those of figure 3.14, where the O spike is greater than the OLi spike.

In KCl, the OLi sample provides a greater photocurrent than the O sample. Again, this is unlikely to be due to light frequency as the differences are marginal, but could be caused by a greater surface area in the OLi sample. This would, however, disagree with the  $\text{Na}_2\text{SO}_3$  result, where the same samples were used. It is possible that this OLi enhancement was due to the NEA of the diamond surface, but this does not account for the increased positive photocurrent at positive potentials when compared to the O sample.

In  $\text{EuCl}_3$  the expected result of an increased negative photocurrent with the OLi sample compared to the O sample is shown. However, this is insufficient evidence for an NEA cause, since this does not particularly agree with the rest of the results presented.

Photocurrent sign changing potentials are affected by the surface termination. In  $\text{EuCl}_3$  they are 0.22 and  $\simeq 0.25$  V, in KCl: 0.09 and 0.24 V and in  $\text{Na}_2\text{SO}_3$ : -0.07 and -0.19 V for OLi and O respectively. These figures correspond to a change on lithiation of -0.03 V in  $\text{EuCl}_3$ , -0.15 V in KCl, and +0.12 V in  $\text{Na}_2\text{SO}_3$ . Reasons for these differences are unclear, but positive changes in the sign changing potential would appear to agree with work that concludes that oxygen terminated diamond has a higher flat band potential than NEA diamond [62, 64].

The presence of surface state effects, confirmed by the photo-activity when illuminated by sub band-gap illumination, was most likely ubiquitous. It was not possible to deduce the exactly nature of the photo-effects causing photocurrent from any of the results presented so far. For example, if surface states exist in the band-gap and contribute to photocurrent, do they work by promoting their electrons to the conduction band, or by having electrons donated from the valence band? It is likely that they are unpopulated under normal conditions due to the Fermi-level suppression

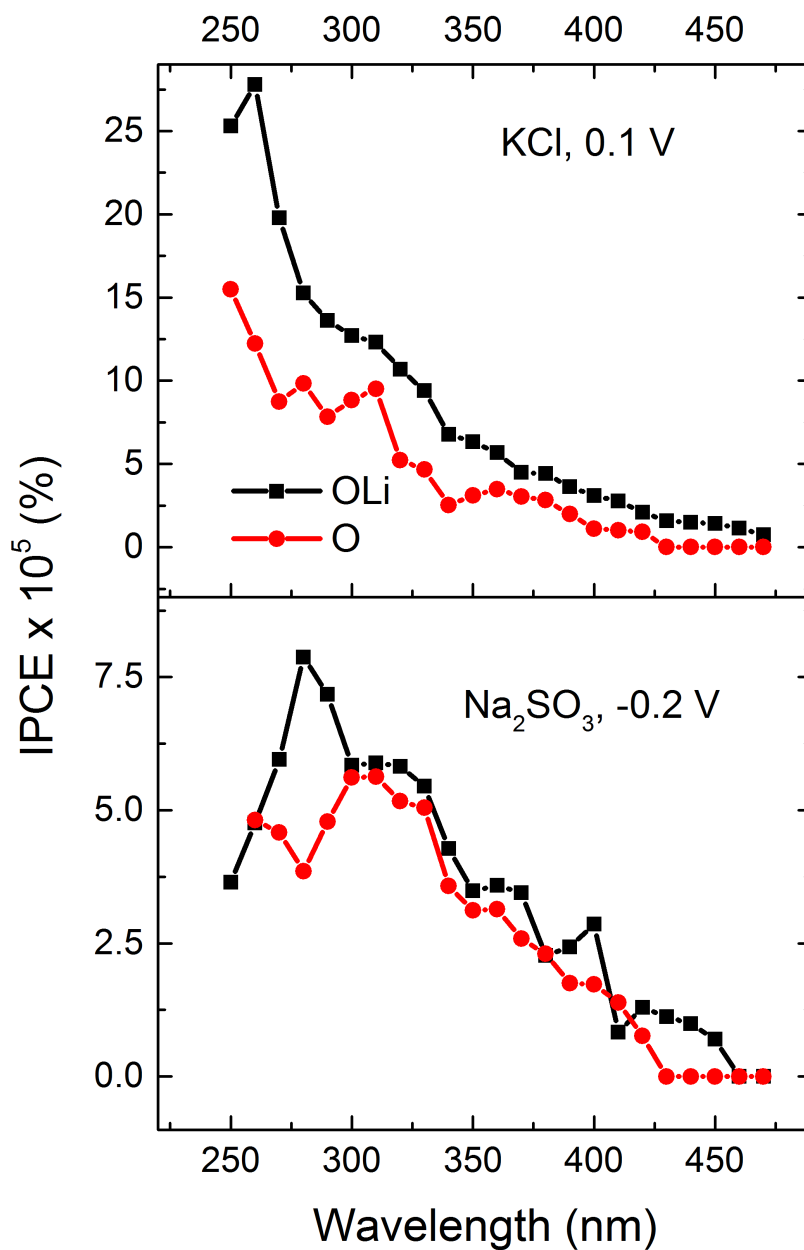


FIGURE 3.18: IPCE-wavelength spectra for O and OLi samples in each electrolyte. Measurements taken by chronoamperometry measurements, converted to an IPCE value and plotted against wavelength (monochromated). All photocurrents measured here were negative. Error bars are excluded for clarity.

in the p-type diamond; however, this is not certain. In addition, what is the energy separation between them and the conduction and valence bands? In order to answer this last question, the monochromator was employed to provide photocurrent measurements at various wavelengths.

### 3.2.5 IPCE-wavelength spectra

Using the monochromated Xe arc lamp, chronoamperometry measurements provided photocurrent data at various wavelengths; this is shown in figure 3.18. The data has been converted to IPCE values using optical power meter data and employing equation 2.2. As a measure of efficiency of a photocurrent system, this can give values that are practical when considering materials for applications. In addition, this figure provides knowledge on the energy of the excitations causing the photocurrent.

As is clear to see from figure 3.18, the onset wavelength for photocurrent is roughly 460 nm. Longer wavelengths gave no photocurrent for any sample studied. At shorter wavelengths the IPCE appears to be reduced, which could be attributed to large errors associated with the drop-off of intensity provided by the Xe arc lamp (see the appendix), and not to a lack of photon-to-charge carrier conversion.

In agreement with the results of figure 3.17, the spectra here conclude that the OLi sample produced photocurrents of greater magnitude than those of O. Both samples produced negative photocurrents, even at positive potentials and in the hole scavenging electrolyte.

The existence of activity in the surface at sub band-gap energies is clear and has an onset energy roughly equal to 2.7 eV (460 nm). This raises the question of substrate-surface  $\text{TiO}_2$ , an n-type semiconductor with a band gap of around 3 eV [86], causing the photocurrent. This could have been produced in the ozone treatment step, as the high energies and presence of  $\text{O}_3$  are strongly oxidising. However, this can be ruled out as the photocurrents produced were entirely negative, indicative of a p-type material, even at small positive potentials as well as in hole scavenging electrolyte.

This is interestingly almost exactly half of the diamond band-gap of 5.45 eV. This suggests that the surface state energies are directly between the valence and conduction bands of the diamond, causing a surface state diagram to be more like figure 3.19 than figure 1.9. If true this implies that holes in the valence band and electrons in the conduction band could both be produced on the surface of the diamond by radiation of the same wavelength. The increase in photocurrent at shorter wavelength might then correspond to both of these processes occurring for more energies, *i.e.* deeper into the valence band and higher into the conduction band.

The dual processes discussed in sections 3.2.1, 3.2.2 and 3.2.3, could according to this hypothesis, be due partly to valence band to surface state excitations, and partly due to surface state to conduction band excitations. Electron mobility in the conduction band is high, whereas in the valence band it is low, and vice-versa for holes. The surface state mobility by definition disallows transport into the bulk. Each of these differences could potentially add up to form a complex excitation and transport process resulting in the presented dual process result.

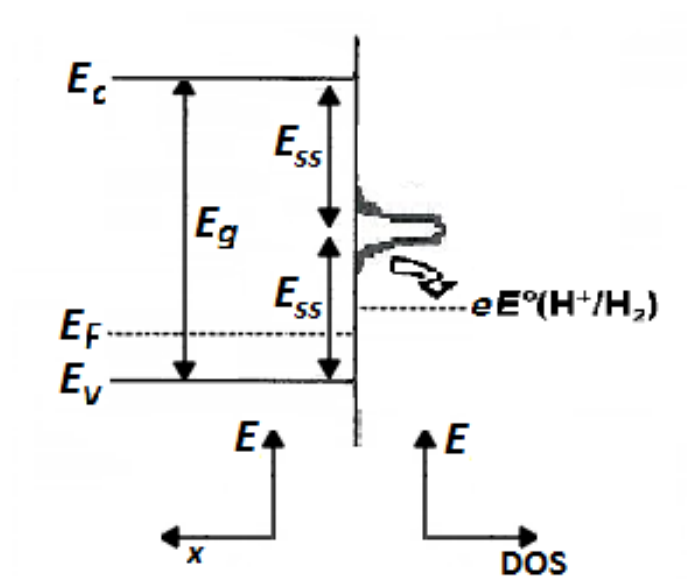


FIGURE 3.19: Schematic of density of surface states (DOS) on a diamond electrode surface.  $E_{SS}$  is now 2.7 eV, making it equally distant in energy to both the valence and the conduction bands.

# Chapter 4

## Conclusion

### 4.1 Summary

HPHT boron-doped diamond particles have been used to fabricate diamond electrodes on titanium substrates suitable for photoelectrochemical water splitting. This followed dynamic light scattering measurements confirming that particle size distribution is lowered by acid treatment, as well as centrifugation, making them suitable for thin-layer self-assembly. It was necessary to optimise several aspects of the self-assembly process, including the use of MPA, the PEI solution concentration and molecular weight, the sonication time and the weight percentage of the diamond suspension, the treatment of the diamond suspension post-sonication, as well as the annealing conditions. This optimisation process yielded positive results in producing thin diamond layers that were chemically bound to the Ti substrate by a Ti/TiC/BDD structure. The diamond surface was terminated with oxygen by ozone treatment, and lithiated by thermal evaporation to produce an NEA surface. This, along with their thin and robust nature, made the electrodes appropriate for use in electro- and photoelectrochemical measurements.

The above fabricated samples were combined with as-received H-terminated, porous Ti/CNT/BDD structured samples. These had varying levels of boron dopant concentration, of the order of  $10^{20}$  to  $10^{21}$  B cm<sup>-3</sup>. When combined with the fabricated samples, which were boron doped to  $10^{21}$  B cm<sup>-3</sup>, these samples constituted a set of four test samples: 0.1H, 0.2H (increasingly doped, Ti/CNT/BDD), OLi and O (Ti/TiC/BDD). These samples were tested in photoelectrochemical environments employing a range of electrolytes, KCl, Na<sub>2</sub>SO<sub>3</sub> and EuCl<sub>3</sub>, and two different light sources, a xenon arc lamp and an argon-mercury discharge tube.

Cyclic voltammetry provided knowledge of the potential window over which the electrodes were stable and initiating no electrochemical processes. In KCl this was  $-0.1 < E < 0.6$  V *vs.* Ag/AgCl, allowing chronoamperometry measurements to be taken in this range. These measurements

employed the Xe lamp, which upon illuminating the sample, induced a measureable photocurrent. This photocurrent appeared to consist of two processes coexisting, and manifesting over different timescales. The different samples showed no conclusive proof of the cause of the ‘spike’ and the ‘decay’. The decay, however, did appear to depend on the termination in the OLi and O samples, suggesting NEA effects.

Upon probing the system in  $\text{Na}_2\text{SO}_3$ , the potential window from CV measurements changed to  $-0.3 < E < 0.15 \text{ V vs. Ag/AgCl}$ . Illumination during chronoamperometry gave little further insight in the new electrolyte, but did confirm the distinct nature of the two processes. Using an Ar-Hg discharge lamp altered the results, shortening the overall timescale and allowing use of lock-in amplification to measure photocurrent-voltage spectra.  $\text{EuCl}_3$  was also introduced as a third electrolyte with an equivalent potential window to KCl.

Photocurrent-voltage spectra showed linear plots of positive gradient, confirming the metallic nature of the diamond. The results did not offer any conclusion that the NEA induced by lithiation stimulated the enhanced reduction of protons. That said, the results showed that the electronic nature of the OLi and O samples were not particularly dissimilar, suggesting the lithiation had not been perfectly completed. Efficiency (IPCE)-wavelength spectra did show that radiation of wavelengths smaller than 460 nm (2.7 eV) produce a photocurrent in diamond. This implies that surface states reside directly between the conduction and valence bands of the diamond surface. Competing and complex processes happening in the surface states under illumination are the most likely cause of the dual process photocurrent responses.

## 4.2 Future Work

**Sample fabrication.** Various techniques to further optimise the fabrication process may give positive results for photoelectrochemistry. For example, the use of diamond suspension pH ranging from 7 up to 11 or 12, which may help to bind the diamond more strongly to the PEI on the substrate surface and therefore give a high surface coverage. In addition, the deposition time (as opposed to letting the suspension dry) could be altered to achieve an even thinner layer. To provide a thinner layer of higher coverage, the particle size segregation could be increased from use of the 30 s centrifugation technique, for example to a multi-step process utilising a more powerful centrifuge. Fine tuning of the annealing conditions in incremental steps upward in temperature and time from 950 °C for 90 s, could further bind the diamond to the substrate without stripping it from the surface.

The self-assembly process could be enhanced by using a smoother Ti surface for deposition. To achieve this, low pressure titanium evaporation onto quartz could be employed. This would result in a smooth and highly clean surface onto which ultra-thin layers of MPA, PEI and BDD could be

more easily deposited. Measures would, however, need to be taken to ensure a conductive contact between the Ti and the rest of the circuit. This may simply involve use of the same conducting silver paint used here.

**Surface treatment.** Infra-red spectroscopy could be employed to probe the specific bonds present on the diamond surface. If oxygen-lithium bonds are present, this would confirm the success of the lithiation process. In addition, with photo-electron spectroscopy techniques it is possible to evaluate the conduction and valence band energies on the diamond surface, further confirming an NEA. The NEA surface can be qualitatively examined in an SEM over a large area, testing the secondary electron emission properties [71]. This technique uses the SEM maximally zoomed out, allowing imaging of (in the SEMs used here) up to four samples. Comparison of their brightness shows the relative electron affinities between samples and across individual samples. NEA surfaces, e.g. H and OLi terminated ones, show clearly brighter images than, for example, O terminated samples. This should be carried out before electrochemical measurements and afterward, to ascertain the effect of electrochemistry on H and OLi terminations.

Self-assembly was used here in order to ensure a high surface area, and a strong adhesion to the Ti substrate. However, CVD could be used to ensure that the facets of diamond are highly exposed during ozone treatment and lithiation. This could enhance the binding of the atoms and help to induce the NEA over a large proportion of the surface.

**Electro- and photoelectrochemistry.** Examination of 3 identical samples, differing only by their surface terminations, would be valuable. This would allow quantitative analysis provided that illumination intensity was kept constant, or was measureable. These samples could be either the Ti/CNT/BDD samples or the Ti/TiC/BDD samples; however, stable termination with O, H and OLi is necessary. Preliminary SEM results for ozone treatment and lithiation of the CNT structured samples showed inconsistent surface coverage of the replacement surface atoms.

Further analysis of the semiconducting properties of the diamond electrodes is necessary. For example Mott-Schottkey analysis of samples with each termination would provide flat-band potentials.

Photoelectrochemical measurements would involve completing the array of measurements carried out here, as well as introducing new experiments. The photocurrent-wavelength spectra could be complimented with further measurements. For example, use of potentials that induce positive photocurrents when measuring photocurrent-wavelength spectra could give insight into the nature of the positive photocurrents, *i.e.* the wavelengths that induce them.

The effects of surface coverage and surface area on photocurrent properties could be analysed. The electrode surface area could be estimated from capacitance measurements, and compared with IPCE data. The as-received squares of BDD (Element 6) could constitute a control sample. As an inherently fully covered surface, these samples give an upper limit to surface coverage.

Their roughness (surface area) could be estimated by capacitance measurements and their outputs compared to the fabricated samples.

A band-gap illumination source in the form of a laser or an LED, providing pure supra-band gap illumination, would be advantageous. This would allow the certain direct inter-band excitation of electrons, to ascertain whether the high energy of the conduction band allows unprecedented potential for reducing solution species [66]. The absorption of band-gap radiation by the air could hinder the use of these sources, as may have been a problem here. However, use of a custom made electrochemical cell with the sample held in close proximity to the quartz window could help solve this issue. In addition, either the cell or light source could be designed with an ultra-low pressure (non-O<sub>2</sub>) gas filled tube, with quartz windows, protruding along the light path. This would allow separation of the lamp and cell, without the loss of the highest energy radiation.

**Beta enhancement.** Use of beta sources to irradiate the electrodes with high energy electrons could also provide interesting results. This would involve replacing the light source with a beta source, potentially inside the electrochemical cell. This could be directly compared to UV light by IPCE measurements and by hydrogen evolution rates. Use of the three different terminations for these measurements would be key, as it is unclear which termination would be most suitable. Considering the unattainable band-gap of diamond to any solar radiation, its NEA characteristics will go unused for renewable water splitting unless a new form of excitation is found. For this reason, further work into the characteristics of diamond for beta-enhanced water splitting is both necessary and exciting.

# Bibliography

- [1] N. Armaroli and V. Balzani. The future of energy supply: challenges and opportunities. *Angew. Chem. Int. Ed.*, 46(1-2):52–66, 2007.
- [2] A. Züttel, A. Borgschulte, and L. Schlapbach. *Hydrogen as a future energy carrier*. Wiley–VCH, 2011.
- [3] A. Züttel, A. Remhof, A. Borgschulte, and O. Friedrichs. Hydrogen: the future energy carrier. *Philos. Trans. R. Soc. London, Ser. A*, 368(1923):3329–3342, 2010.
- [4] J. Yang, A. Sudik, C. Wolverton, and D. J. Siegel. High capacity hydrogen storage materials: attributes for automotive applications and techniques for materials discovery. *Chem. Soc. Rev.*, 39(2):656–675, 2010.
- [5] T. Lipman. An overview of hydrogen production and storage systems with renewable hydrogen case studies. *Clean Energy States Alliance Report*, 2011.
- [6] N. S. Lewis and D. G. Nocera. Powering the planet: Chemical challenges in solar energy utilization. *Proc. Natl. Acad. Sci. U.S.A.*, 103(43):15729–15735, 2006.
- [7] P. A. Lessing. A review of sealing technologies applicable to solid oxide electrolysis cells. *J. Mater. Sci.*, 42(10):3465–3476, 2007.
- [8] A. Brisse, J. Schefold, and M. Zahid. High temperature water electrolysis in solid oxide cells. *Int. J. Hydrogen Energy*, 33(20):5375–5382, 2008.
- [9] F. Barbir. Pem electrolysis for production of hydrogen from renewable energy sources. *Sol. Energy*, 78(5):661–669, 2005.
- [10] S. A Grigoriev, V. I. Porembsky, and V. N. Fateev. Pure hydrogen production by PEM electrolysis for hydrogen energy. *Int. J. Hydrogen Energy*, 31(2):171–175, 2006.
- [11] J. L. Sawin and REN21. *Renewables 2011: Global status report*. Worldwatch Institute Washington, DC, 2011.
- [12] K. Maeda and K. Domen. Photocatalytic water splitting: recent progress and future challenges. *J. Phys. Chem. Lett.*, 1(18):2655–2661, 2010.

- [13] Z. Liu, W. Hou, P. Pavaskar, M. Aykol, and S. B. Cronin. Plasmon resonant enhancement of photocatalytic water splitting under visible illumination. *Nano Lett.*, 11(3):1111–1116, 2011.
- [14] A. Fujishima and K. Honda. Electrochemical photolysis of water at a semiconductor electrode. *Nature*, 238(5385):37–38, 1972.
- [15] M. A. Lazar, S. Varghese, and S. S. Nair. Photocatalytic water treatment by titanium dioxide: Recent updates. *Catalysts*, 2(4):572–601, 2012.
- [16] M. Ni, M. K. H. Leung, D. Y. C. Leung, and K. Sumathy. A review and recent developments in photocatalytic water-splitting using  $\text{TiO}_2$  for hydrogen production. *Renewable Sustainable Energy Rev.*, 11(3):401–425, 2007.
- [17] P. Silija, Z. Yaakob, V. Suraja, N. N. Binitha, and Z. S. Akmal. An enthusiastic glance in to the visible responsive photocatalysts for energy production and pollutant removal, with special emphasis on titania. *Int. J. Photoenergy*, 2012, 2011.
- [18] M. Pelaez, N. T. Nolan, S. C. Pillai, M. K. Seery, P. Falaras, A. G. Kontos, P. S. M. Dunlop, J. W. J. Hamilton, J. Byrne, K. O’Shea, M. H. Entezari, and D. D. Dionysiou. A review on the visible light active titanium dioxide photocatalysts for environmental applications. *Appl. Catal., B*, 125:331–349, 2012.
- [19] Z. Chen, H. N. Dinh, and E. Miller. *Photoelectrochemical Water Splitting*. Springer, 2013.
- [20] K. E. Spear and J. P. Dismukes. *Synthetic diamond: emerging CVD science and technology*, volume 25. John Wiley & Sons, 1994.
- [21] J. A. Garrido, M. Nesládek, and K. Haenen. Fundamentals and applications of diamond. *Phys. Status Solidi A*, 209(9):1607–1608, 2012.
- [22] W. A. Harrison. *Electronic structure and the properties of solids: the physics of the chemical bond*. Courier Dover Publications, 2012.
- [23] J. Wilks and E. Wilks. *Properties and applications of diamond*. Butterworth-Heinemann Oxford, 1991.
- [24] H. M. Ledbetter. Stainless-steel elastic constants at low temperatures. *J. Appl. Phys.*, 52(3):1587–1589, 1981.
- [25] L. S. Pan and D. R. Kania. *Diamond: electronic properties and applications*, volume 294. Springer, 1995.
- [26] W. M. Haynes. *CRC handbook of chemistry and physics*. CRC press, 2012.
- [27] P. W. May. Diamond thin films: a 21st-century material. *Philos. Trans. R. Soc. London, Ser. A*, 358(1766):473–495, 2000.

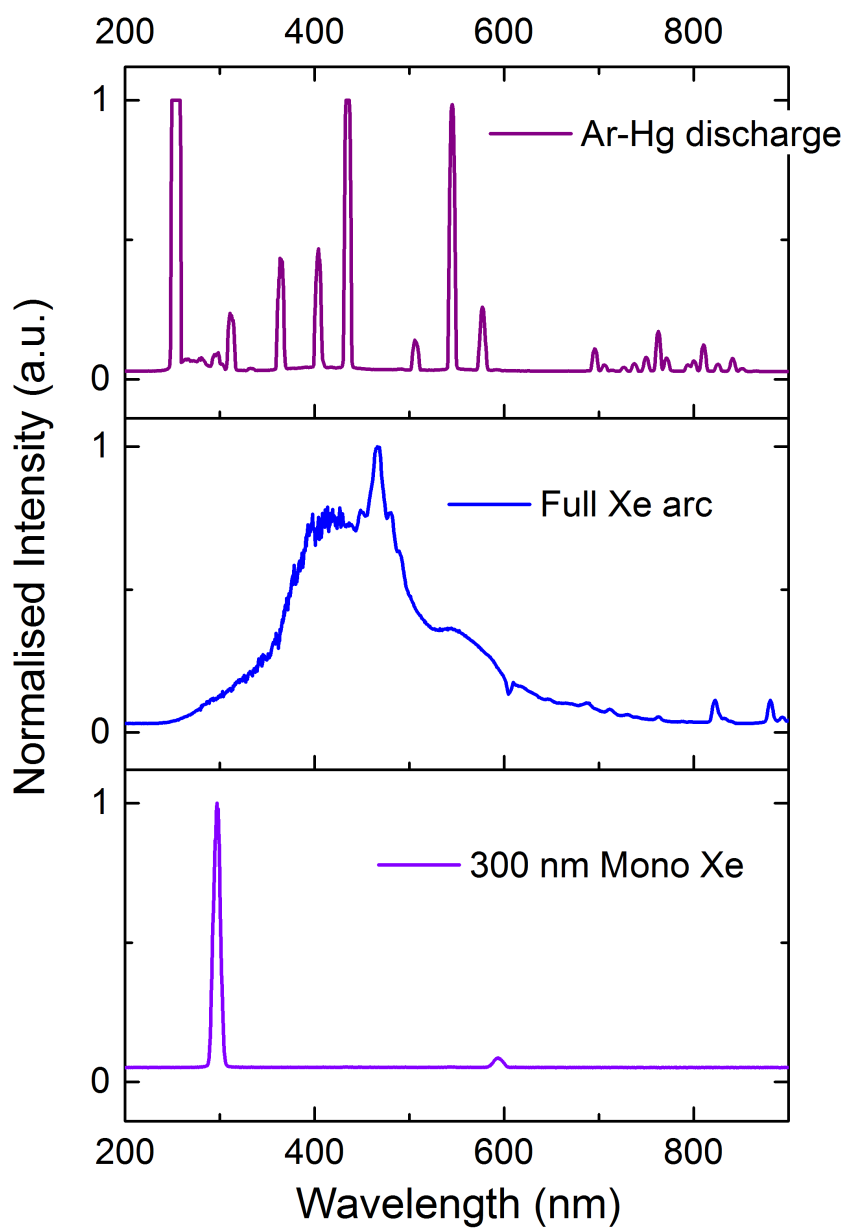
- [28] A. Paoletti and A. Tucciarone. *The Physics of Diamond*, volume 135. IOS Press, 1997.
- [29] M. Schwander and K. Partes. A review of diamond synthesis by cvd processes. *Diamond Relat. Mater.*, 20(9):1287–1301, 2011.
- [30] A. Bazargan, Y. Yan, D. C. W. Hui, and G. McKay. A review: Synthesis of carbon-based nano and micro materials by high temperature and high pressure. 2013.
- [31] V. Y. Dolmatov. Detonation synthesis ultradispersed diamonds: properties and applications. *Russ. Chem. Rev.*, 70(7):607, 2001.
- [32] A. M. Zaitsev. *Optical properties of diamond: a data handbook*. Springer, 2001.
- [33] R. Kalish. Diamond as a unique high-tech electronic material: difficulties and prospects. *J. Phys. D: Appl. Phys.*, 40(20):6467, 2007.
- [34] R. Mildren and J. Rabeau. *Optical Engineering of Diamond*. John Wiley & Sons, 2013.
- [35] S. Koizumi and M. Suzuki. n-type doping of diamond. *Phys. Status Solidi A*, 203(13):3358–3366, 2006.
- [36] H. Kato, T. Makino, S. Yamasaki, and H. Okushi. n-type diamond growth by phosphorus doping on (0 0 1)-oriented surface. *J. Phys. D: Appl. Phys.*, 40(20):6189, 2007.
- [37] P. W. May. The new diamond age? *Science*, 319(5869):1490–1491, 2008.
- [38] D. A. Tryk, A. Fujishima, and K. Honda. Recent topics in photoelectrochemistry: achievements and future prospects. *Electrochim. Acta*.
- [39] J. van der Weide, Z. Zhang, P. K. Baumann, M. G. Wensell, J. Bernholc, and R. J. Nemanich. Negative-electron-affinity effects on the diamond (100) surface. *Phys. Rev. B*, 50(8):5803, 1994.
- [40] X. Blase, E. Bustarret, C. Chapelier, T. Klein, and C. Marcenat. Superconducting group-iv semiconductors. *Nat. Mater.*, 8(5):375–382, 2009.
- [41] T. Frauenheim, U. Stephan, P. Blaudeck, D. Porezag, H.-G. Busmann, W. Zimmermann-Edling, and S. Lauer. Stability, reconstruction, and electronic properties of diamond (100) and (111) surfaces. *Phys. Rev. B*, 48(24):18189, 1993.
- [42] P. W. May, J. C. Stone, M. N. R. Ashfold, K. R. Hallam, W. N. Wang, and N. A. Fox. The effect of diamond surface termination species upon field emission properties. *Diamond Relat. Mater.*, 7(2):671–676, 1998.
- [43] J. O’M. Bockris and S. U. M. Khan. *Surface Electrochemistry: A Molecular Level Approache*. Springer, 1993.

- [44] J. B. Cui, J. Ristein, and L. Ley. Electron affinity of the bare and hydrogen covered single crystal diamond (111) surface. *Phys. Rev. Lett.*, 81(2):429, 1998.
- [45] A. J. Neves and M. H. Nazaré. *Properties, growth and applications of diamond*. Number 26. IET, 2001.
- [46] S. M. Sze and K. K. Ng. *Physics of semiconductor devices*. John Wiley & Sons, 2006.
- [47] S. Mohammadi and C. R. Selvakumar. Calculation of depletion layer thickness by including the mobile carriers. *IEEE Trans. Electron Devices*, 43(1):185–188, 1996.
- [48] M. G. Walter, E. L. Warren, J. R. McKone, S. W. Boettcher, Q. Mi, E. A. Santori, and N. S. Lewis. Solar water splitting cells. *Chem. Rev.*, 110(11):6446–6473, 2010.
- [49] D. B. Hibbert. *Introduction to Electrochemistry*. Macmillan Press, 1993.
- [50] R. White. *Modern Aspects of Electrochemistry*. Springer Science, 2009.
- [51] E. Gileadi. *Physical Electrochemistry: Fundamentals, Techniques, and Applications*, volume 1. Wiley-VCH, 2011.
- [52] A. Mills and S. Le Hunte. An overview of semiconductor photocatalysis. *J. Photochem. Photobiol., A*, 108(1):1–35, 1997.
- [53] W. W. Gärtner. Depletion-layer photoeffects in semiconductors. *Phys. Rev.*, 116(1):84, 1959.
- [54] L. S. Pan and D. R. Kania. *Diamond: electronic properties and applications*, volume 294. Springer, 1994.
- [55] E. Yasu, N. Ohashi, T. Ando, J. Tanaka, M. Kamo, Y. Sato, and H. Kiyota. Hall mobility and carrier concentration of boron-doped homoepitaxially grown diamond (001) films. *Diamond Relat. Mater.*, 4(1):59–61, 1994.
- [56] T. Bak, J. Nowotny, M. Rekas, and C. C. Sorrell. Photo-electrochemical hydrogen generation from water using solar energy. materials-related aspects. *Int. J. Hydrogen Energy*, 27(10): 991–1022, 2002.
- [57] X. Wang, S.-B. Che, Y. Ishitani, and A. Yoshikawa. Systematic study on p-type doping control of InN with different Mg concentrations in both In and N polarities. *Appl. Phys. Lett.*, 91(24): 242111–242111, 2007.
- [58] C. Kittel and P. McEuen. *Introduction to solid state physics*, volume 8. Wiley New York, 2005.
- [59] Y. V. Pleskov, A. Y. Sakharova, M. D. Krotova, L. L. Bouilov, and B. V. Spitsyn. Photoelectrochemical properties of semiconductor diamond. *J. Electroanal. Chem. Interfacial Electrochem.*, 228(1):19–27, 1987.

- [60] K. Patel, K. Hashimoto, and A. Fujishima. Photoelectrochemical investigations on boron-doped chemically vapour-deposited diamond electrodes. *J. Photochem. Photobiol., A*, 65(3):419–429, 1992.
- [61] L. Boonma, T. Yano, D. A. Tryk, K. Hashimoto, and A. Fujishima. Observation of photocurrent from band-to-band excitation of semiconducting p-type diamond thin film electrodes. *J. Electrochem. Soc.*, 144(6):L142–L145, 1997.
- [62] T. N. Rao, D. A. Tryk, K. Hashimoto, and A. Fujishima. Band-edge movements of semiconducting diamond in aqueous electrolyte induced by anodic surface treatment. *J. Electrochem. Soc.*, 146(2):680–684, 1999.
- [63] Y. V. Pleskov, V. M. Mazin, Y. E. Evstefeeva, V. P. Varnin, I. G. Teremetskaya, and V. A. Laptev. Photoelectrochemical determination of the flatband potential of boron-doped diamond. *Electrochem. Solid-State Lett.*, 3(3):141–143, 2000.
- [64] I. Yagi, K. Tsunozaki, D. A. Tryk, and A. Fujishima. Control of the dynamics of photogenerated carriers at the boron-doped diamond/electrolyte interface by variation of the surface termination. *Electrochem. Solid-State Lett.*, 2(9):457–460, 1999.
- [65] D. MyungáJang, H. SoonáIm, Y. JaeáCho, and C. WooáLee. Nanodiamonds as photocatalysts for reduction of water and graphene oxide. *Chem. Comm.*, 48(5):696–698, 2012.
- [66] D. Zhu, L. Zhang, R. E. Ruther, and R. J. Hamers. Photo-illuminated diamond as a solid-state source of solvated electrons in water for nitrogen reduction. *Nat. Mater.*, 12(9):836–841, 2013.
- [67] M. Grätzel. Photoelectrochemical cells. *Nature*, 414(6861):338–344, 2001.
- [68] K. Honda, T. N. Rao, D. A. Tryk, A. Fujishima, M. Watanabe, K. Yasui, and H. Masuda. Electrochemical characterization of the nanoporous honeycomb diamond electrode as an electrical double-layer capacitor. *J. Electrochem. Soc.*, 147(2):659–664, 2000.
- [69] H. G. Zanin, P. W. May, D. J. Fermin, D. Plana, S. M. C. Vieira, W. I. Milne, and E. J. Corat. Porous boron-doped diamond/carbon nanotube electrodes.
- [70] K. M. O’Donnell, T. L. Martin, N. A. Fox, and D. Cherns. Ab initio investigation of lithium on the diamond c (100) surface. *Phys. Rev. B*, 82(11):115303, 2010.
- [71] T. L. Martin. *Lithium oxygen termination as a negative electron anity surface on diamond: a computational and photoemission study*. PhD thesis, University of Bristol, 2011.
- [72] J. Furthmüller, J. Hafner, and G. Kresse. Structural and electronic properties of clean and hydrogenated diamond (100) surfaces. *Europhys. Lett.*, 28(9):659, 1994.
- [73] F. Maier, J. Ristein, and L. Ley. Electron affinity of plasma-hydrogenated and chemically oxidized diamond (100) surfaces. *Phys. Rev. B*, 64(16):165411, 2001.

- [74] P. Bergonzo, D. Tromson, and C. Mer. Radiation detection devices made from cvd diamond. *Semicond. Sci. Technol.*, 18(3):S105, 2003.
- [75] O. Avila, A. E. Buenfil, and M. E. Brandan. Diamond tl response to alpha, beta and gamma radiation. *Radiat. Prot. Dosim.*, 58(1):61–63, 1995.
- [76] H. Zanin, P. W. May, M. H. M. O. Hamanaka, and E. J. Corat. Field emission from hybrid diamond-like carbon and carbon nanotube composite structures. *ACS Appl. Mater. Interfaces*, 5(23):12238–12243, 2013.
- [77] S. Xu, P. E. Laibinis, and G. Liu. Accelerating the kinetics of thiol self-assembly on gold a spatial confinement effect. *J. Am. Chem. Soc.*, 120(36):9356–9361, 1998.
- [78] O. K. Varghese and C. A. Grimes. Appropriate strategies for determining the photoconversion efficiency of water photoelectrolysis cells: a review with examples using titania nanotube array photoanodes. *Sol. Energy Mater. Sol. Cells*, 92(4):374–384, 2008.
- [79] J. L. Davidson, W. D. Brown, A. Gicquel, B. V. Spitsyn, and J. C. Angus. *Diamond Materials VI*, volume 1. The Electrochemical Society, 2000.
- [80] A. Krüger, F. Kataoka, M. Ozawa, T. Fujino, Y. Suzuki, A. E. Aleksenskii, A. Y. Vul, and E. Ōsawa. Unusually tight aggregation in detonation nanodiamond: identification and disintegration. *Carbon*, 43(8):1722–1730, 2005.
- [81] E. Buccioni, E. Braca, J. M. Kenny, and M. L. Terranova. Processing–structure–adhesion relationship in cvd diamond films on titanium substrates. *Diamond Relat. Mater.*, 8(1):17–24, 1999.
- [82] P. R. Thornton. *Scanning electron microscopy: applications to materials and device science*. Chapman and Hall, 1968.
- [83] E. Skavas, A. Adriaens, and T. Hemmingsen. A comparative study of sulphite oxidation under alkaline conditions by use of wall-jet flow cell and rotating disc electrode. *Int. J. Electrochem. Sci.*, 1(8):414–424, 2006.
- [84] P. M. S. Monk. *Physical chemistry: understanding our chemical world*. John Wiley and Sons, 2008.
- [85] J. W. M. De Backer and C. M. J. De Bie. Low-pressure mercury discharge lamp, November 28 1995. US Patent 5,471,113.
- [86] S. U. M. Khan, M. Al-Shahry, and W. B. Ingler. Efficient photochemical water splitting by a chemically modified n-TiO<sub>2</sub>. *Science*, 297(5590):2243–2245, 2002.

# Appendix



UV-vis spectra of the lamps used in photoelectrochemical measurements. Top: the argon-mercury discharge tube. Middle: the xenon arc lamp. Bottom: the xenon arc lamp with 300 nm monochromation.